Enhancing Microgrid Resilience: A Robust Protection Strategy Employing Differential & Overcurrent Relays

Devendra Mangre, Kunal Sawalakhe
Tulsiramji Gaikwad Patil College of Engg. and Tech.
Nagpur, Mahrashtr
✉ devendra.mangre@gmail.com

Mohan Thakre
SVERI's College of Engineering
Pandharpur

ABSTRACT

This article introduces a novel method to enhance the protection scheme for micro grid systems experiencing significant transitions between islanded and grid operating modes. In order to handle the dynamic variations in short-circuit fault current characteristics, the suggested hybrid flexible protection system strategically includes both over current and differential relays. Adaptive over current relays are employed to safeguard distributed generators (DGs) and individual load points (LPs), while differential relays are utilized to protect feeders, backbone lines, and buses. This novel approach seeks to lessen the need for infrastructure upgrades and the complexity of setting computations.

The protection scheme operates adaptively, utilizing over current relays for faults outside the protection zone and employing differential relays for faults within the designated zone. This approach ensures the safety of consumers and equipment connected within the micro grid system network. Time-domain simulations with a standard microgrid test network in the MATLAB/Simulink software environment are used to validate the suggested strategy. This research contributes to advancing the resilience and effectiveness of micro grid systems in dynamic operational scenarios.

KEYWORDS *: Adaptive over current relay, Short circuit fault current, Islanded mode, Distributed generators, Reliability enhancement, Efficiency improvement, Stability, Protection zone.*

INTRODUCTION

In the realm of grid modernization and the integration of DG sources, micro grids have emerged as a focal point. Characterized as medium- or low-voltage networks encompassing local loads and DG sources, micro grids offer the flexibility to operate in grid-connected and islanded modes based on the presence of a utility connection [1]. The proliferation of DG sources in microgrids brings forth advantages such as loss reduction, prevention of network congestion, and increased resilience through islanded operation [2].

However, the integration of DG sources introduces operational and protection challenges, deviating from the conventional design principles of distribution networks depend on large SC currents & radial power flow [3].

Notably, topological changes in microgrids during transitions between grid and islanded conditions pose challenges in short-circuit behavioral changes, affecting protection infrastructure. The key issue arises when a microgrid shifts to an islanded condition, leading to a significant reduction in short circuit levels due to the absence of a utility supply [4]. This is especially relevant in microgrids with DG sources that are mostly inverter-based and that have current-limiting devices installed, since this could make the current overcurrent protection insufficient [5].

Adaptive overcurrent protection, a dynamic process modifying protective responses in response to system changes, employs microprocessor-based directional overcurrent relays (DOCR) for microgrid protection. DOCRs offer flexibility with selectable tripping curves tailored to specific system needs. Implementation of adaptive protection can follow centralized or decentralized control approaches, each demanding

distinct communication architectures [6]. Microgrid protection encounters challenges during transitions between grid-connected and islanded modes, leading to short circuit level variations. Adaptation to these changes is critical; however, traditional solutions, such as adding storage units, prove impractical due to high costsand uncertain fault-clearing times [7].

The bidirectional power flow in microgrids, a consequence of distributed generator (DG) connections and mesh configurations, introduces new protection challenges. Power electronic converters in DGs, operating in intermittent and current-limiting environments, pose additional complexities. Meshed networks, while enhancing reliability, present communication challenges that impact effective protection [8-10]. In addressing these complexities, adaptive protection schemes emerge as effective solutions for microgrids operating in diverse modes. A proposed hybrid protection safeguarding feeders, buses, and load points. Communication links are optional, considering cost and complexity concerns [11-12].

Several studies propose adaptive protection methods for low-voltage microgrids, utilizing communication links for efficient fault detection and relay coordination. While these systems provide reliable and fast operation, communication failures remain unaddressed [13]. Alternatives, such as storage-based systems using flywheels, present challenges in on-time fault clearing and require substantial installations [14].

The core challenge in adaptive relaying lies in adjusting relay settings based on load behavior, manner of functioning and production levels. Directional over current relays face coordination difficulties in multi-source and multi-loop networks due to varied current flow directions. Overcoming these challenges necessitates the development of efficient and fast adaptive overcurrent protection systems [15-16].

IMPACTS OF DG ON POWER SYSTEMS: A COMPREHENSIVE ANALYSIS

"Incorporating Distributed Generators (DG) into distribution networks yields a spectrum of effects, both advantageous and detrimental. When addressing faults in the distribution system, overcurrent protection plays a pivotal role. However, the introduction of DG alters the overall fault current perceived by the relay, triggering shifts in operation time and potential structural concerns [17]. This change in fault current, influenced by the DG's location, can either elevate or diminish, leading to adjusted relay operation times and potential challenges.

The escalation of nominal current flow raises concerns about falsified tripping, given that relays are typically configured to safeguard a specific section termed the relay reach, determined by the minimal level Ipickup. The presence of DG curtails this reach and diminishes the overall fault current. Consequently, the relay might fail to detect currents from buses below Ipickup, categorizing them as beyond the protection system's reach [18].

Figure 1 visually depicts the influence of DG on relay reach. In the absence of DG, the relay reverts to its initial reach. However, the identification of DG presence diminishes the relay reach, occasionally falling below the actual reach. The collective impact of DG, fault resistance (RF), and DG location from the power source collectively shape the relay reach.

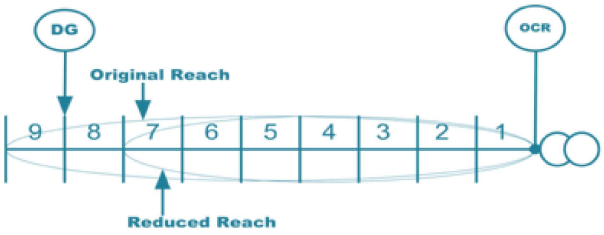

Figure 1 Assessment of original and reduced reach

Adjustments to thresholds for Short Circuit (SC) and fault current (If) become imperative due to the modified venin impedance of the system resulting from DG attachment. Fault current levels fluctuate based on the parallel association of DGs with machinery, impacting the system's configuration [19-20]. Lower fault currents may render the fault undetectable, especially when they are below load currents. Additionally, the grounding connections of transformers and generators contribute to distinguishing DG faults from asymmetrical faults.

DG interactions pose challenges to overcurrent relays, particularly in bidirectional fault scenarios where multiple switches may need activation for fault removal. This intricacy necessitates additional switching devices and protective measures for overcurrent relays,

rendering them susceptible to false tripping due to changes in fault currents [21].

INTEGRATED APPROACH: CONFIGURATION, AND METHODOLOGY

Recent advancements in microgrid protection underscore the need for integrating cost-effective wireless sensor networks (WSN) and multifunctional microprocessor-based relays. Noteworthy challenges include issues with current transformer (CT) mismatches, CT saturation leading to erroneous measurements, and the the complex multi-terminal component differential protection adjustment.

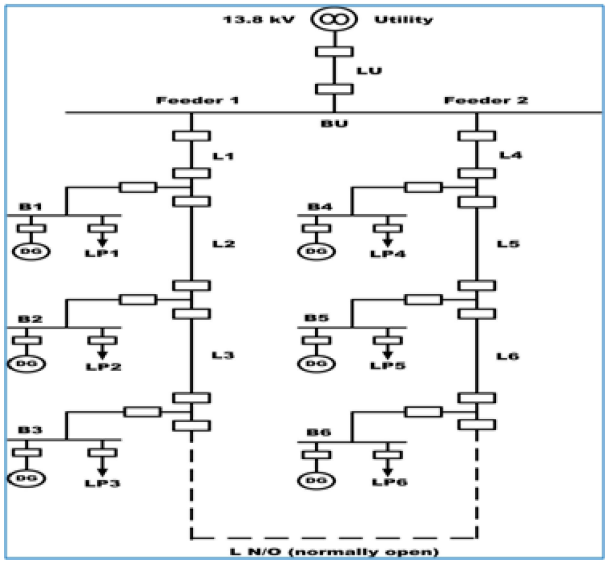

Figure 2: Study system

In response to the identified challenges, there emerges a compelling need for a holistic solution in the form of an integrated over current adaptive relay and differential relay protection scheme tailored for smart microgrid systems [22]. This envisioned protection system must possess dynamic adaptability to grid changes, incorporating self-monitoring and self-healing capabilities. Leveraging AI methods, the microprocessor/numerical relay technology should optimize and adapt seamlessly [23]. The protection strategy must be customized for various zones and equipment within the microgrid, ensuring cost-effectiveness, reliability, and efficiency in both autonomous and grid-connected modes [24]. A test microgrid system as depicted in Figure 2. Subsequent sections delve into a meticulous examination of the load flow within the AC microgrid system for both operational modes.

System Parameters

Utility grid-rated capacity = 13.8 kV; DG1 to DG6 rating = 0.2 MW; The power factor for all DGs = 0.9; Load points LP1, LP2, LP4, LP5 rating = 0.2 MW; Load points LP3, LP6 rating = 0.1 MW; The power factor for all load points (LPs) = 0.9 [31]

RESULTS AND DISCUSSIONS

AC Microgrid System with One DG Connection

The 3-phase sinusoidal voltage and current measurement in normal operating conditions in the microgrid system are done by using the 2 scope blocks connected to the 3-phase V-I measurement bus bar. This microgrid system model is formed in the MATLAB/Simulink software environment.

Normal Operating Condition

Figure 3 shows the microgrid system model with one DG connection in normal operating conditions.

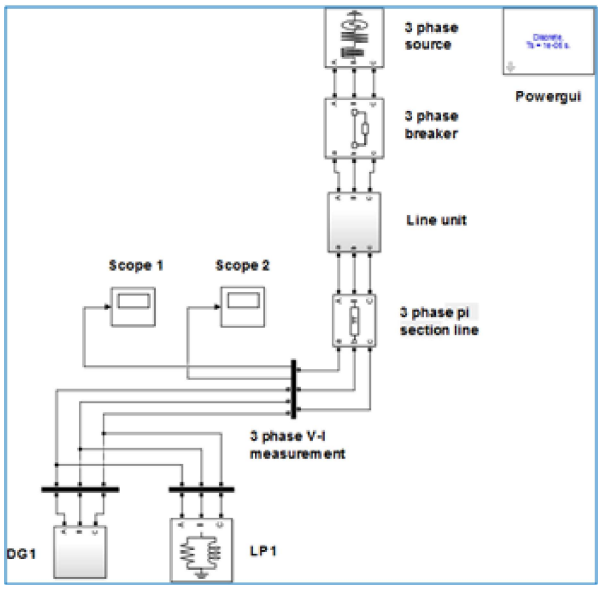

Figure 3: Microgrid system with one DG connection in normal operating condition

Figure 4 shows the load flow report table for the microgrid system with one DG connection in normal operating conditions. In this table, the load flow for one

3-phase source, one 3-phase RLC load, and one bus are shown.

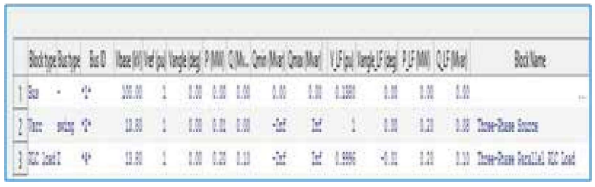

Figure 4: Load flow report of the microgrid system with one DG connection in normal operating condition

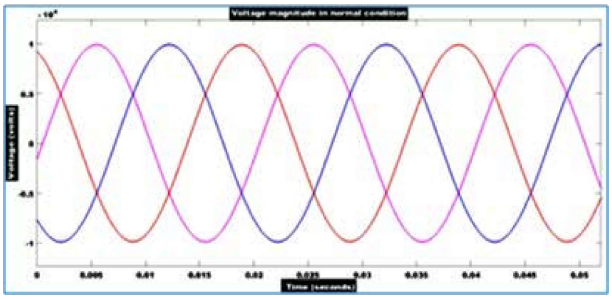

Figure 5: Voltage magnitude in normal operating condition

In these results, Figure 5 shows the 3-phase sinusoidal voltage magnitude when the microgrid system is operating in grid-connected mode and the normal condition with the 50 Hz frequency, and Figure 6 shows the 3-phase sinusoidal current magnitude condition with the 50 Hz frequency.

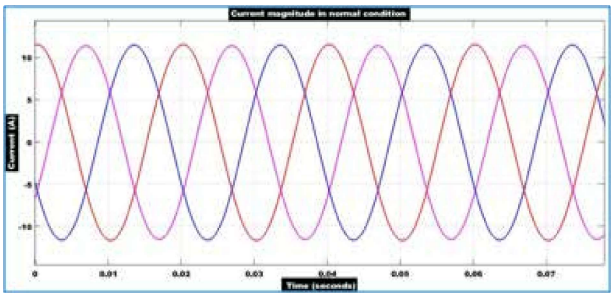

Figure 6: Current magnitude in normal operating condition

Faulty Condition

In this type of fault, the magnitudes of the voltage of the 3 phases which are short-circuited with each other drop down to the zero value instantaneously. Whereas, the current of 3 faulted phases with each other increases instantaneously to the maximum value.

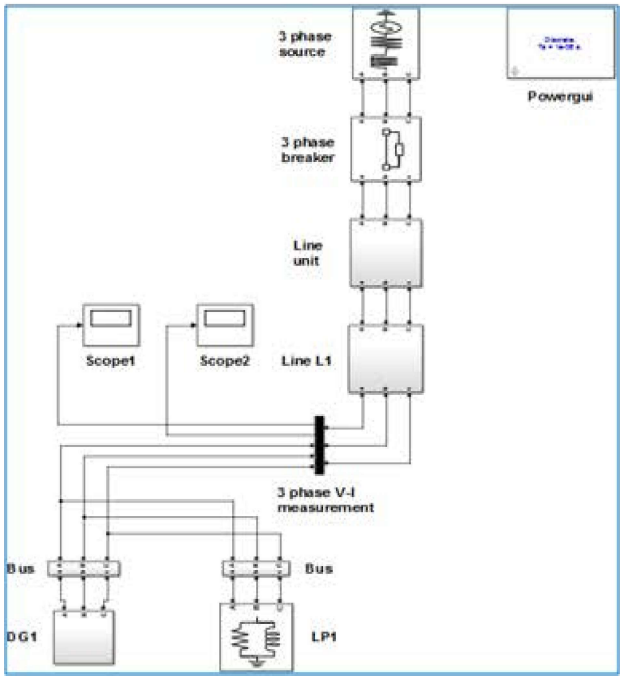

Figure 7: Microgrid system with one DG connection for LLL fault on line L1

Figure 7 shows the microgrid system model with one DG connection when LLL fault has occurred on line L1. The 3ss-phase sinusoidal voltage and current measurement before and after the LLL fault occurrence on line L1 in the microgrid system are done by using the 2 scope blocks connected to the 3-phase V-I measurement bus bar.

Figure 8 shows the load flow report table for the microgrid system with one DG connection for an LLL fault that occurred on line L1. In this table, the load flow for one 3-phase source, one 3-phase RLC load, and three buses are shown.

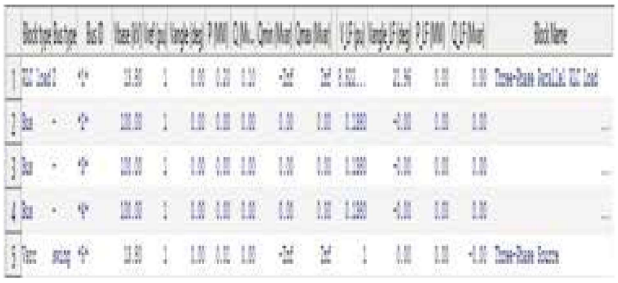

Figure 8: Load flow report with one DG connection for LLL fault on line L1

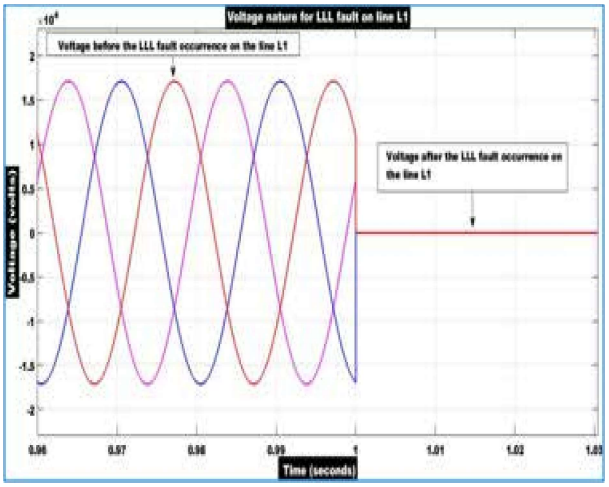

Figure 9: Voltage nature for LLL fault on line L1 before and after the fault occurrence

Figure 9 shows the 3-phase voltage magnitude for the LLL fault on line L1 before and after the fault occurrence with the 50 Hz frequency. In this result, initially, when the microgrid system is operated in the normal operating condition the 3-phase voltage is sinusoidal in nature from 0 to 1 second. The magnitude of this sinusoidal voltage before the fault occurrence is up to 170 kV from 0 to 1 second in normal operating conditions. But, when 3 phase SC LLL fault is occurred on the line L1 at 1 second that time voltage of all three phases drops to zero instantaneously due to this LLL fault on the line L1. The voltage of these three phases remains zero till the LLL fault is cleared completely on line L1 in the microgrid system.

Figure 10 shows the 3-phase sinusoidal current magnitude for the LLL fault on line L1 before and after the fault occurrence with the 50 Hz frequency. In this result, initially, when the microgrid system is operated in the normal operating condition the 3-phase current is sinusoidal in nature with 10 to 15 A current magnitudes from 0 to 1 second. But, when 3 phase SC LLL fault occurs on line L1 at 1 second that time two phases' current magnitude increases up to 78 A instantaneously, and current of the remaining phase also increases up the 24 A instantaneously due to the LLL fault on the line L1. This current magnitude remains high till the LLL fault is cleared completely on line L1 in the microgrid system.

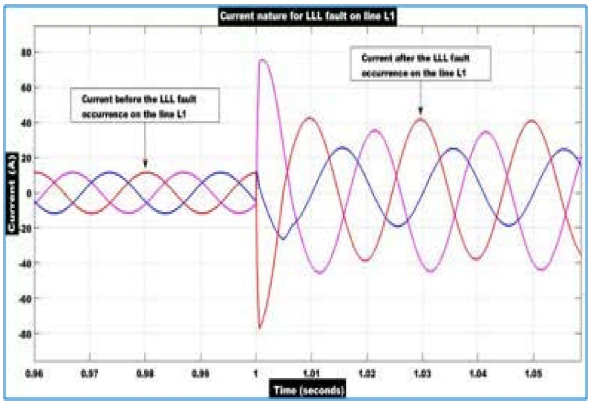

Figure 10: Current nature of LLL fault on line L1 before and after the fault occurrence

In LLLG type of fault, the magnitude of the voltage of the 3 phases which are short-circuited with each other with the ground drops down to the zero value instantaneously. Whereas, the current of 3 faulted phases with each other with the ground increases instantaneously to the maximum value.

Case Study - 1: Protecting an AC microgrid system using a current differential relay protection scheme in the event of a three-phase single LLG fault occurring on line L1 in both modes of operation (protecting faults occurring within the protected zone of the microgrid structure, such as faults on feeders, lines, buses, etc.).

Case Study - 2 Protecting an AC microgrid system by implementing an adaptive overcurrent relay protection scheme. This scheme is designed to respond to a 3-phase SC LLLG fault occurring at the 3-phase parallel RLC load point LP1, in both modes of operation.

Current Differential Relays for AC Microgrid Protection (Case Study 1

Figure 11 illustrates the intricate model of the microgrid system in the grid-connected mode of operation.

In the grid-connected state of execution, the table for the load flow assessment of the microgrid system is shown in Figure 12 Each bus's load flow computation is included in this table. All of the components' block names, types, and bus IDs are listed here. The three-phase RLC source, bus, and load points' base voltages are also displayed in this table. Each bus's reference voltage in pu is displayed.

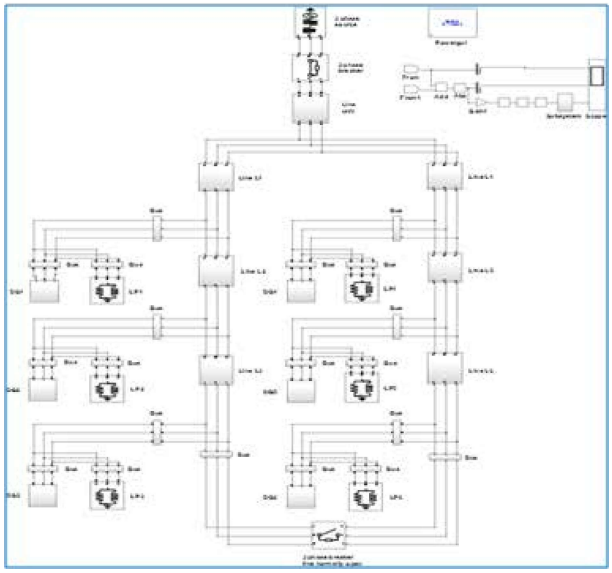

Figure 11: Micro grid system in grid-connected

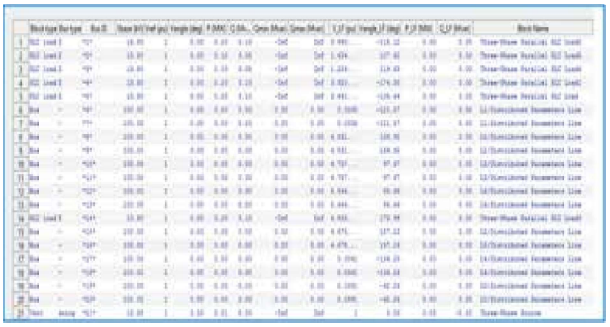

Figure 12: Load flow for grid-connected

RESULTS

When run in a grid-connected state, the microgrid network produces the outcomes shown in Figure 13 On the three-phase line L1, a three-phase LLLG fault is generated at 0.1 seconds, and three outcomes are displayed. This safeguards the microgrid system's customers and machinery from three-phase faults that happen within the designated zone (such as those at feeders, lines, buses, etc.). Using the existing differential relay protection technique, these faults are eliminated in 0.1 to 0.2 s.

According to this outcome, up until 0.1 seconds before the fault occurs, the current flowing through radial breaker unit 1 (RBU1) is constant. Within 0.1 seconds of the fault occurring on line L1, the current waveform of the RBU1 current drops precipitously, reaching -2000 A current in a remarkably brief amount of time. The RBU1 current signal returns to its stable zero condition and continues to do so in a straight line for up to 0.2 seconds after the current differential relay has been successfully operated.

Differential Current-RBU1 and B1BU, the Radial Breaker Units

The differential current in this scenario is initially flowing in a straight line from zero to 0.1 seconds before the fault occurs. However, the differential relay trips the corresponding circuit breaker after 0.1 seconds when a fault occurs at 0.1 seconds, after which line L1 flows at a maximum differential current of 875 A.

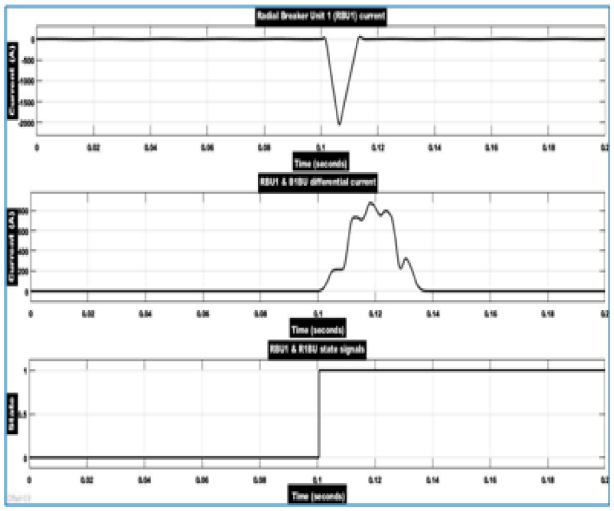

Figure 13: grid-connected mode

State signals of the Radial breaker unit 1 (RBU1) and the radial 1 breaker unit (R1BU).

This outcome is the consequence of a straight-line state signal flow from the zero location up to 0.1 seconds, emanating from the circuit breaker units RBU1 and R1BU. Following the 0.1-second fault occurrence, the RBU1 and R1BU state signals ascend to state 1, and then remain in a steady upward flow until the fault is entirely cleared on the line L1 unit, which occurs at 0.2 seconds after state 1.

Adaptive Overcurrent Relays for AC Microgrid Protection (Case Study - 2)

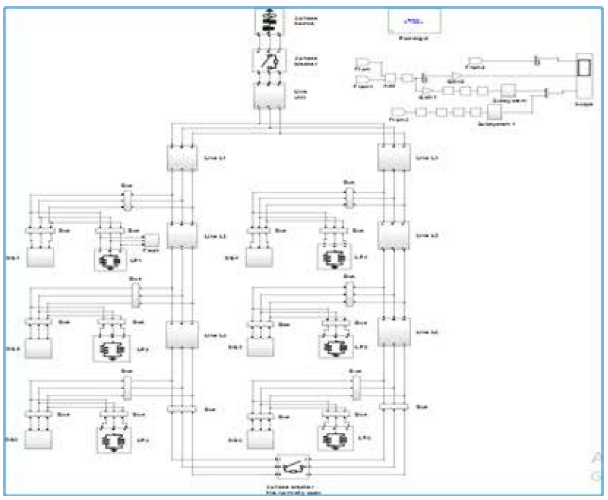

Figure 14: Islanded mode

Figure 14 offers an intricate view of the microgrid system's model during the islanded mode of operation.

The detailed load flow analysis is presented in Figure 15.

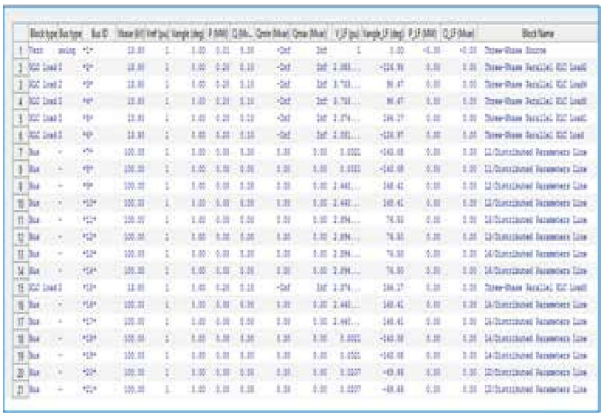

Figure 15: Load flow

The load flow report also encompasses base voltage values, reference voltages, active and reactive power calculations, as well as voltage load flow and angle measurements. These calculations, derived from the power GUI block of the microgrid system's model during islanded operation, contribute to a thorough understanding of the system's performance.

Results during the Island Mode of Operation

The presented Figure 16 illustrates the outcomes during the microgrid system's islanded mode of operation. The adaptive overcurrent relay protection scheme successfully clears these faults within the timeframe of 0.1 to 0.2 seconds, ensuring the safety and reliability of the microgrid system.

Load Point 1 (LP1) Current

The adaptive overcurrent relay registers LP1 current peaking at 2250 A for a brief 1 to 1.5 cycle duration. Following fault clearance on LP1, the current stabilizes and flows consistently from 0.14 to 0.2 seconds.

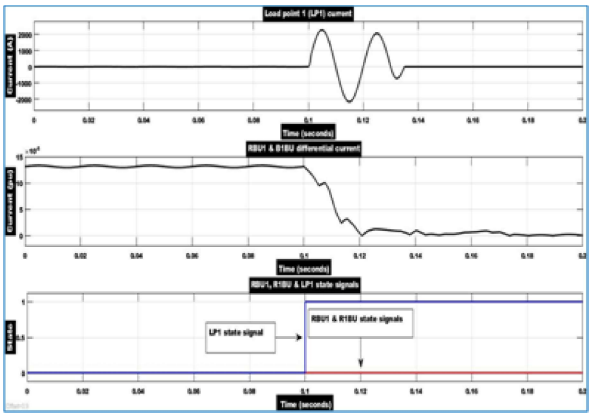

Figure 16: Islanded mode

CONCLUSION

This paper concludes that this protection scheme for the microgrid system under the study operated effectively and protected the overall microgrid system from 3 phases of SC symmetrical LLLG faults are occurred in both grid-connected and islanded modes of operation. Also, the adaptive overcurrent relays protection scheme operated successfully and protected the consumers as well as equipment connected in the microgrid system.

Also, this microgrid protection scheme shows feasibility and effectiveness in both modes of operation under the changing SC fault current level and varying fault impedance in the microgrid system. This protection scheme can be effectively implemented for symmetrical faults like LLL, and LLLG faults. This protection scheme improves the reliability, power quality, efficiency, and safety operation of both consumers as well as equipment connected to the microgrid system by clearing the 3-phase SC faults in the minimum possible time and by protecting the overall microgrid system effectively.

REFERENCES

1. M. R. Islam and H. A. Gabbar, "Analysis of microgrid protection strategies," in 2012 International Conference on Smart Grid (SGE), Aug 2012.
2. M. A. Zamani, T. S. Sidhu, and A. Yazdani, "A protection strategy and microprocessor-based relay for low-voltage microgrids," IEEE Transactions on Power Delivery, vol. 26, no. 3, July 2011.
3. P. Gupta, R. S. Bhatia, and D. K. Jain, "Adaptive protection schemes for the microgrid in a smart grid scenario: Technical challenges," in 2013 IEEE Innovative Smart Grid Technologies-Asia (ISGT Asia), Nov 2013.
4. P. Mahat, Z. Chen, B. Bak-Jensen, and C. L. Bak, "A simple adaptive overcurrent protection of distribution systems with distributed generation," IEEE Transactions on Smart Grid, vol. 2, Sep. 2011.
5. N. P. Matale, "Alleviation of Voltage Sag-Swell by DVR Based on SVPWM Technique," 2020 Int. Conf. on Power, Energy, Control and Transmission Systems (ICPECTS), 2020, pp. 1-6, doi: 10.1109/ICPECTS49113.2020.9336972.
6. H. Wan, K. K. Li, and K. P. Wong, "An adaptive multiagent approach to protection relay coordination with distributed generators in industrial power distribution system," IEEE Transactions on Industry Applications, vol. 46, 2010.
7. E. Sortomme, S. S. Venkata, and J. Mitra, "Microgrid protection using communication-assisted digital relays," IEEE Transactions on Power Delivery, vol. 25, Oct 2010.
8. Y. Han, X. Hu, and D. Zhang, "Study of adaptive fault current algorithm for microgrid dominated by inverter-based distributed generators," in The 2nd International Symposium on Power Electronics for Distributed Generation Systems, June 2010.
9. B. Hussain, S. M. Sharkh, S. Hussain, and M. A. Abusara, "Integration of distributed generation into the grid: Protection challenges and solutions," in 10th IET International Conference on Developments in Power System Protection (DPSP 2010). Managing the Change, March 2010.
10. P. R. Khade, "Optimal Reach Settings of Mho Relay for Series Compensated Transmission Line Protection," 2020 4th Int. Conf. on Electronics, Communication and Aerospace Technology (ICECA), 2020, pp. 307-313, doi: 10.1109/ICECA49313.2020.9297516.
11. D. Turcotte and F. Katiraei, "Fault contribution of grid-connected inverters," in 2009 IEEE Electrical Power Energy Conference (EPEC), Oct 2009.
12. T. S. Ustun, C. Ozansoy, and A. Zayegh, "A central microgrid protection system for networks with fault current limiters," in 2011 10th International Conference on Environment and Electrical Engineering, May 2011.
13. Ahmad, A. Interline Power Flow Controller (IPFC) Deployment in Long Transmission Lines and its Effects on Distance Relay. J. Inst. Eng. India Ser. B 103, 491–505 (2022). https://doi.org/10.1007/s40031-021-00637-y
14. H. Miller, J. Burger, N. Fischer, and B. Kasztenny, "Modern line current differential protection solutions," in 2010 63rd Annual Conference for Protective Relay Engineers, March 2010.
15. S. Kar, S. R. Samantaray, and M. D. Zadeh, "Data-mining model-based intelligent differential microgrid protection scheme," IEEE Systems Journal, vol. 11, no. 2, June 2017.
16. E. Casagrande, W. L. Woon, H. H. Zeineldin, and D. Svetinovic, "A differential sequence component protection scheme for microgrids with inverter-based distributed generators," IEEE Transactions on Smart Grid, vol. 5, no. 1, Jan 2014.
17. Vijay S. Kale, "An adaptive approach for three-zone operation of digital distance relay with Static Var Compensator using PMU," Int. Journal of Ele. Power & Energy Systems, Vol. 77, 2016, pp. 327-336, SSN 0142-0615, https://doi.org/10.1016/j.ijepes.2015.11.049.
18. H. J. Laaksonen, "Protection principles for future microgrids," IEEE Transactions on Power Electronics, vol. 25, no. 12, Dec 2010.
19. D. Bejmert, W. Rebizant, and L. Schiel, "Differential protection restraining procedures for objects with more than two supply ends," in 45th International Universities Power Engineering Conference UPEC2010, Aug 2010.
20. K. A. Wheeler, S. O. Faried, and M. Elsamahy, "A microgrid protection scheme using differential and adaptive overcurrent relays," in 2017 IEEE Electrical Power and Energy Conference (EPEC), Oct 2017.

21. Kumar, N. Evaluation and Control Perceptive of VSM-Based Multilevel PV-STATCOM for Distributed Energy System. MAPAN 36, 561–578 (2021). https://doi.org/10.1007/s12647-021-00481-x

22. F. Motabarian, M. A. Golkar, and S. Hajiaghasi, "Surveying the effect of distributed generation on over current protection in radial distribution systems," in 18th Electric Power Distribution Conference, April 2013.

23. "IEEE guide for the application of current transformers used for protective relaying purposes - redline," IEEE Std C37.110-2007 (Revision of IEEE Std C37.110-1996) - Redline, April 2008.

24. H. Sonawane and M. Thakre, "Modified Distance Protection for Series Compensated (SC) Overhead Lines," 2021 Third Int. Conf. on Intelligent Communication Technologies and Virtual Mobile Networks (ICICV), 2021, pp. 468-474, doi: 10.1109/ICICV50876.2021.9388506.

Empowering Microgrids Protection Through Adaptive Relays

Devendra Mangre, Kunal Sawalakhe
Tulsiramji Gaikwad Patil College of Engg. and Tech.
Nagpur, Mahrashtr
✉ devendra.mangre@gmail.com

Mohan Thakre
SVERI's College of Engineering
Pandharpur

ABSTRACT

This research introduces an innovative hybrid adaptive protection system for microgrid systems, enhancing resilience during transitions between grid and islanded modes. Integrating overcurrent and differential relays strategically, the system addresses dynamic variations in short-circuit fault current characteristics. Adaptive overcurrent relays protect DGs and individual LPs, while differential relays safeguard feeders, backbone lines, and buses, aiming to minimize infrastructure upgrades and simplify setting computations. Through rigorous simulations covering diverse operating conditions, the proposed scheme proves effective in shielding the microgrid from substantial three-phase short-circuit fault currents, enhancing reliability, efficiency, power quality, and stability. Operating adaptively, the scheme uses overcurrent relays for faults outside the protection zone and differential relays for faults within the specified zone, ensuring the safety of consumers and equipment in the microgrid network. Validation through simulations on a typical microgrid test network in MATLAB/Simulink significantly contributes to advancing microgrid system resilience and effectiveness in dynamic operational scenarios.

KEYWORDS *: Differential relay, Microgrid operation, Grid-connected mode, Islanded mode, Load points, Reliability enhancement, Power quality assurance, Stability optimization.*

Abbreviations & Nomenclature

MG	Microgrid
IM	Islanded Mode
C.T	Current Transformers
R1BU	Radial 1 Breaker Unit
GCM	Grid Connected Mode
RF	Fault Resistance
B	Bus
AOCRP	Adaptive Overcurrent Relay Protection
MPPT	Maximum Power Point Tracking
Length of line	L1, L2, L3, L4, L5, L6, and LU = 0.5 km
ADN	Active distribution networks
DRP	Differential Relay Protection
LLL	3 Phase Short circuit faults

INTRODUCTION

While research on protection schemes for microgrids is in its early stages, adaptive protection schemes have been proposed, albeit with inherent complexities. Adaptive protection requires advanced technology, self-monitoring capabilities, and complex integration of hardware and software units, demanding significant upgrades to existing infrastructure for practical implementation [1]. Existing protection methods, such as differential schemes utilizing communicative relays, demand extensive communication infrastructure and relay deployment at each line end [2]. In this challenging landscape, this research introduces a hybrid protection scheme, combining differential and adaptive overcurrent relays. The scheme employs differential relays to safeguard microgrid feeders, lines, and interconnecting buses, while adaptive overcurrent relays protect DGs and individual load points.

The integration of DGs into the main grid to form a microgrid offers a viable alternative, leveraging renewable sources for reduced transmission losses, improved power quality, and environmental sustainability [3-5]. The operation of microgrids can be categorized into four modes, each presenting unique challenges to traditional protection coordination schemes. Fault currents becoming bi-directional, limitations imposed by inverter-based DGs, and variations in fault current

levels due to different generator types contribute to the ineffectiveness of conventional relays [6-7]. Adaptive protection's automatic adjustment to power system conditions and the inherent advantages of differential protection make this hybrid approach promising for addressing the complexities of microgrid protection [8].

As microgrids continue to evolve, necessitating dynamic protection solutions, this research explores the integration of adaptive and differential protection schemes to enhance the reliability and efficiency of microgrid protection systems. Several studies propose adaptive protection methods for low-voltage microgrids, utilizing communication links for efficient fault detection and relay coordination [9-11]. While these systems provide reliable and fast operation, communication failures remain unaddressed [12]. Alternatives, such as storage-based systems using flywheels, present challenges in on-time fault clearing and require substantial installations [13].

CHALLENGES IN EXISTING ADAPTIVE OVERCURRENT RELAY APPROACHES

The current landscape of AOCR schemes faces critical challenges, particularly in light of evolving distributed energy resource (DER) interconnection requirements and the dynamic transition to microgrid operations.

Existing AOCR schemes encounter difficulties in accurately estimating fault current contributions from DERs operating at varying output levels. Traditional approaches, treating DERs as constant current sources, may lead to overcompensation or underreaching due to the complex nature of DER behavior [14]. These challenges arise from factors like distance from the fault, fault impedance, and fault type, making it imperative to refine AOCR schemes to account for changing fault current contributions [15].

Delayed Trip Time in Microgrid Mode

Microgrids, characterized by lower fault currents compared to grid-connected systems, pose a unique challenge to AOCR sensitivity in primary/secondary protection zones. The traditional time-based coordination methods may introduce significant delays in relay trip times for faults within the primary zone, an aspect often overlooked in existing AOCR approaches [16].

Current Direction Reversal during Mode Switching

The possibility of current direction reversal, a phenomenon observed during mode switching in both grid-connected systems and microgrids, remains inadequately addressed in existing AOCR approaches. [17]. These approaches are susceptible to under-reaching, struggle with changing fault currents, and may prove overly complex for traditional distribution relays. The subsequent section delves into an emerging vulnerability that challenges conventional practices in relay programming [18].

PROTECTION STRATEGIES FOR MICROGRIDS

Differential protection involves assessing the electrical quantities entering and leaving a designated security zone by comparing current through CTs. This method relies on either current balance or voltage balance to determine the absence of faults [19].

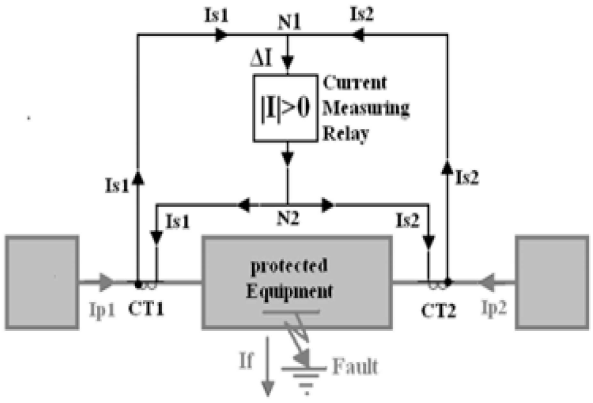

Fig. 1 Current Balance Differential protection

The evolution of relay protection began with high-current relay protection, from which the Discriminatory Short Circuit Protection (DSCP) scheme emerged. DSCP differs from 'overload' protection, incorporating time-based relay operation to safeguard devices thermally. The AOCR Protection system, derived from DSCP, addresses challenges in microgrid operation modes, adapting to distinct short circuit attributes [20].

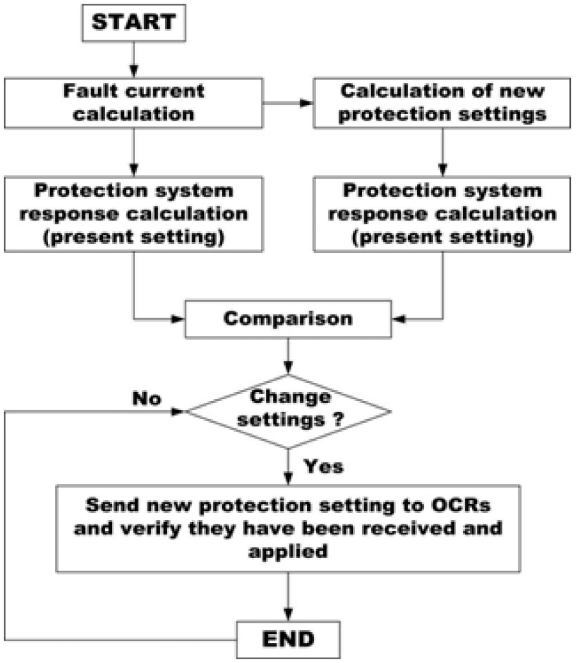

Fig. 2: Adaptive overcurrent protection algorithm

AOCRP accommodates these complexities by enabling adjustments based on grid conditions, facilitated through external communication technology [21]. However, incorporating microgrid configurations into the relay introduces inherent inefficiencies, particularly in intricate network structures, potentially leading to malfunctions during unforeseen events [22].

Adaptive Protection Scheme: Fig. 2 illustrates an adaptive protection scheme with two approaches.

The first approach responds to alterations in the network, adjusting configurations, linking or disconnecting DGs, and transitioning between islanded and grid-connected modes. This approach involves real-time calculation and modification of settings, requiring robust decision-making capabilities [20].

PROBLEM STATEMENT AND SYSTEM DESCRIPTION

This envisioned protection system must possess dynamic adaptability to grid changes, incorporating self-monitoring and self-healing capabilities. The protection strategy must be customized for various zones and equipment within the microgrid, ensuring cost-effectiveness, reliability, and efficiency.

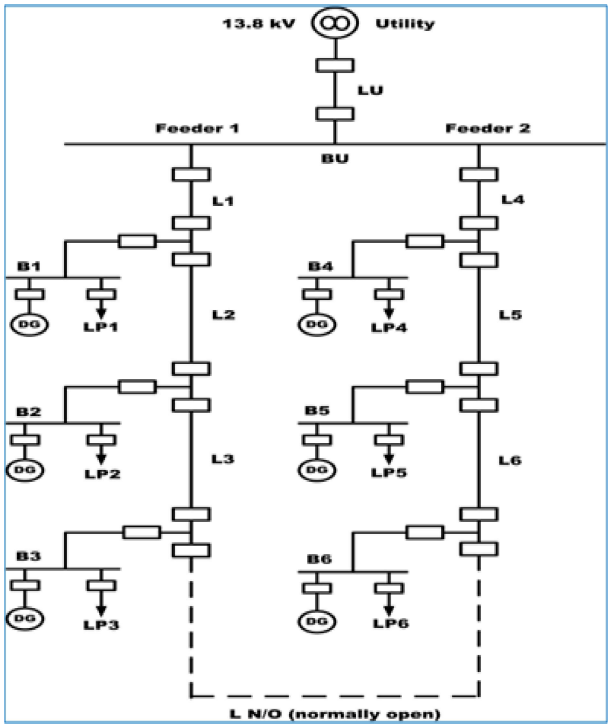

Fig. 3 System under study

This research paper is dedicated to securing the AC microgrid system in both grid-connected and islanded modes, employing a test microgrid system as depicted in Fig 3. Subsequent sections delve into a meticulous examination of the load flow within the AC microgrid system for both operational modes.

System Parameters:

Utility grid-rated capacity = 13.8 kV; DG1 to DG6 rating = 0.2 MW; The power factor for all DGs = 0.9; Load points LP1, LP2, LP4, LP5 rating = 0.2 MW; Load points LP3,; LP6 rating = 0.1 MW; The power factor for all load points (LPs) = 0.9

Protection Settings:

Line and bus differential relay CT ratio = 150/5; Load points CT ratio = 150/5; IDIFFPKP MIN = 0.05pu (0.25A); IBreakpoint = 1pu (5A); K1 = 20%; K2 = 98%

Grid mode:

FINDINGS AND EXPLORATION

In the AC electrical power distribution network like a power system network or microgrid system operating in

both modes of operation in normal operating conditions the 3-phase voltage and current waveforms are sinusoidal in nature with a 50 Hz frequency. But, when 3-phase symmetrical short circuit (SC) faults like LLL, LLLG, or unsymmetrical short circuit (SC) faults like LG, LL, and LLG have occurred in the power system or microgrid system operating in both modes of operation then the magnitude of the SC voltage VSC is decreased to the zero or nearest to the zero value and SC fault current ISC is increased to the very high value in a very short period.

Abnormal Operating Condition

Fig. 4 shows the microgrid system model with one DG connection when 3-phase faults occurred on line L1. The 3-phase sinusoidal voltage and current measurement before and after the fault occurrence on line L1 in the microgrid system is done by using the 2 scope blocks connected to the 3-phase V-I measurement bus bar. This microgrid system model is formed in the MATLAB/ Simulink software environment.

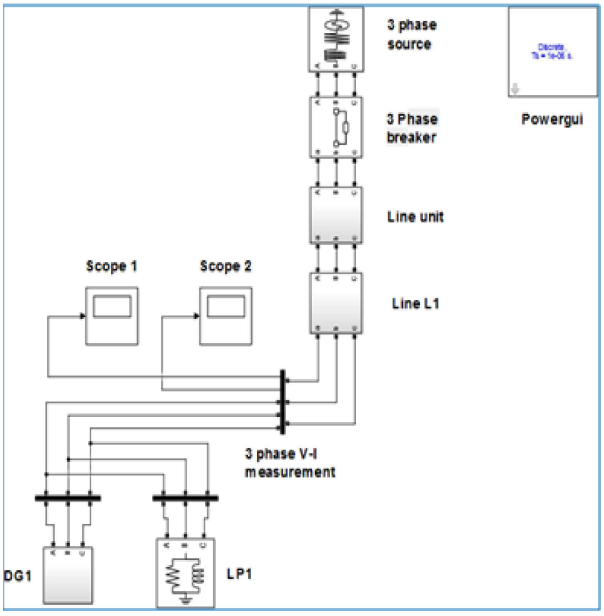

Fig. 4: Microgrid system with one DG connection in faulty condition

This diagram shows the load flow report table for the microgrid system with one DG connection in the faulty condition. In this table, the load flow for one 3-phase source, one 3-phase RLC load, and two buses are shown.

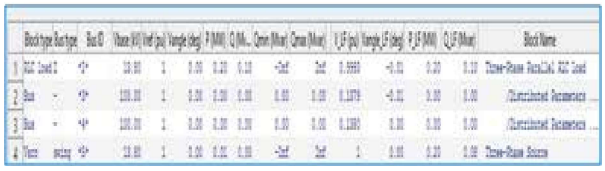

Fig. 5: Load flow report of the microgrid system with one DG connection in faulty condition

Fig. 6 shows the 3-phase voltage magnitude before and after the fault occurrence on the line L1 with the 50 Hz frequency. In this result, initially, when the microgrid system is operated in the normal operating condition the 3-phase voltage is sinusoidal in nature from 0 to 1 second. The magnitude of this sinusoidal voltage is up to 10 kV from 0 to 1 second in the normal condition. But, when 3 phase SC fault is occurred on the line L1 at 1 second that time 3 phase voltage magnitude suddenly drops to the zero value. This voltage magnitude remains zero till the fault is cleared completely on line L1 in the microgrid system.

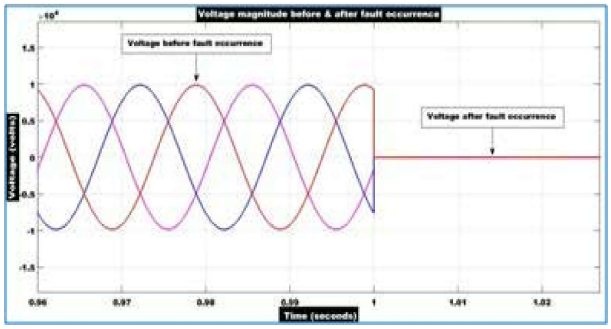

Fig. 6: Voltage magnitude before and after the fault occurrence

Fig. 7 shows the 3-phase sinusoidal current magnitude before and after the fault occurrence on the line L1 with the 50 Hz frequency. In this result, initially, when the microgrid system is operated in the normal operating condition the 3-phase current is sinusoidal in nature with a small current magnitude from 0 to 1 second. But, when 3 phase SC fault occurs on the line L1 at 1 second that time 3 phase current magnitude drastically increases to a very large amount. This current magnitude remains high till the fault is cleared completely on line L1 in the microgrid system.

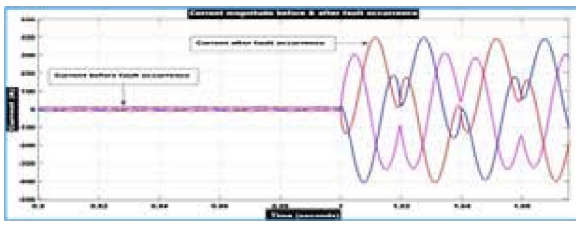

Fig. 7: Current magnitude before and after the fault occurrence

Microgrid System with One DG Connection for LLG Fault on Line L1

In this section, the voltage and current magnitude nature concerning the time domain for various symmetrical and unsymmetrical faults that occurred in the AC microgrid system are discussed. The voltage of the phase where the fault occurs instantaneously drops to zero value and current increases to the maximum value after the fault occurrence at that phase. The microgrid system model for any of these symmetrical or unsymmetrical faults is formed in the MATLAB/Simulink software environment, load flow reports are taken from the powerful block and results for each of the faults are shown for validation and discussion purposes. Fig. 8 shows the microgrid system model with one DG connection when an LLG fault has occurred on line L1.

The 3-phase sinusoidal voltage and current measurement before and after the fault occurrence on line L1 in the microgrid system is done by using the 2 scope blocks connected to the 3-phase V-I measurement bus bar. This microgrid system model is formed in the MATLAB/ Simulink software environment.

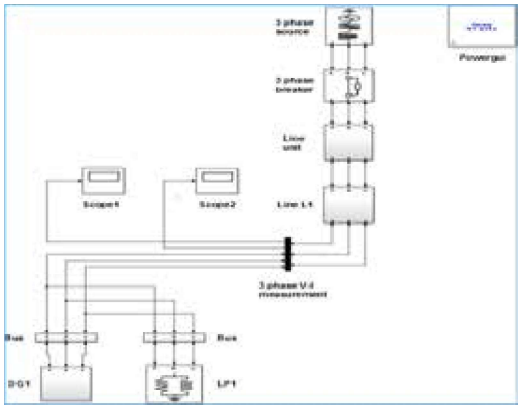

Fig. 8: Microgrid system with one DG connection for LLG fault on line L1

Fig. 9 shows the load flow report table for the microgrid system with one DG connection for the LLG fault that occurred on line L1. In this table, the load flow for one 3-phase source, one 3-phase RLC load, and three buses are shown.

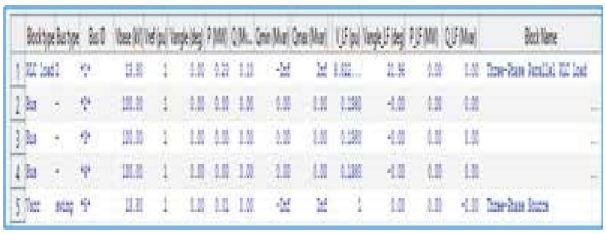

Fig 9: Load flow report of the microgrid system with one DG connection for LLG fault on line L1

Fig 10 shows the 3-phase voltage magnitude for the LLG fault on line L1 before and after the fault occurrence with the 50 Hz frequency. In this result, initially, when the microgrid system is operated in the normal operating condition the 3-phase voltage is sinusoidal in nature from 0 to 1 second.

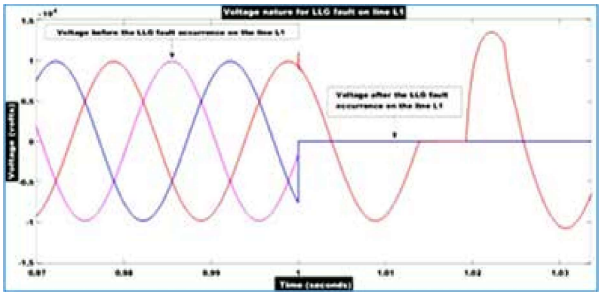

Fig. 10: Voltage nature for LLG fault on line L1 before and after the fault occurrence

The magnitude of this sinusoidal voltage before the fault occurrence is up to 10 kV from 0 to 1 second in normal operating conditions. But, when 3 phase SC LLG fault occurred on line L1 at 1 second that time voltage of the two phases dropped to zero instantaneously and the remaining one-phase voltage increased up to 1.14 kV sinusoidally due to this LLG fault on line L1. The voltage of these two phases remains zero till the LLG fault is cleared completely on line L1 in the microgrid system.

Fig 11 shows the 3-phase sinusoidal current magnitude for LLG fault on line L1 before and after the fault occurrence with the 50 Hz frequency.

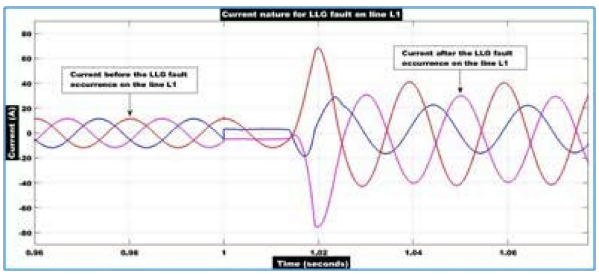

Fig. 11: Current nature for LLG fault on line L1 before and after the fault

In this result, initially, when the microgrid system is operated in the normal operating condition the 3-phase current is sinusoidal in nature with 10 to 15 A current magnitudes from 0 to 1 second. But, when 3 phase SC LLG fault occurs on line L1 at 1 second that time two phases' current magnitude increases up to 70 A in a very small-time duration and the current of the remaining phase also increases up the 30 A in a small-time duration due to the LLG fault on the line L1. This current magnitude remains high till the LLG fault is cleared completely on line L1 in the microgrid system.

Microgrid System with One DG Connection for LLLG Fault on Line L1

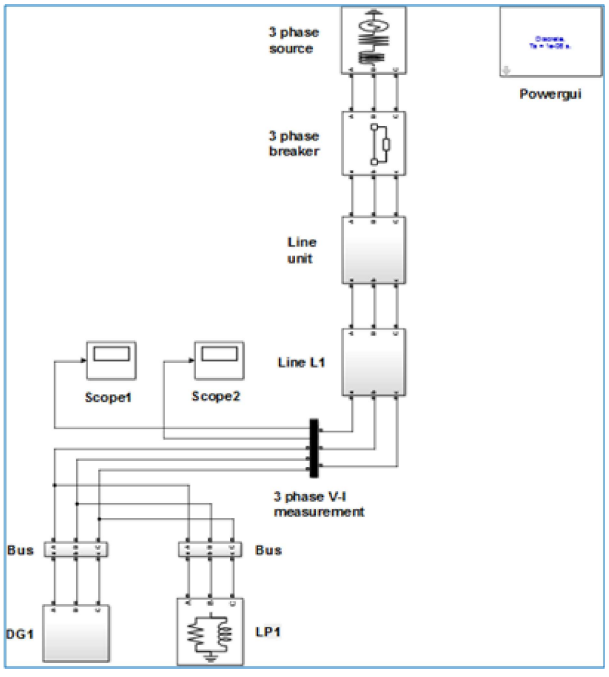

Fig 12: Microgrid system with one DG connection for LLLG fault on line L1

Fig 12 shows the microgrid system model with one DG connection when an LLLG fault has occurred on line L1. In this model, the microgrid system is operated in the grid-connected mode of operation with one 0.2 MW DG and one 0.2 MW parallel RLC load point (LP) connected in parallel with the DG at the lower end of the power distribution buses. The 3-phase sinusoidal voltage and current measurement before and after the LLLG fault occurrence on line L1 in the microgrid system is done by using the 2 scope blocks connected to the 3-phase V-I measurement bus bar. This microgrid system model is formed in the MATLAB/Simulink software environment.

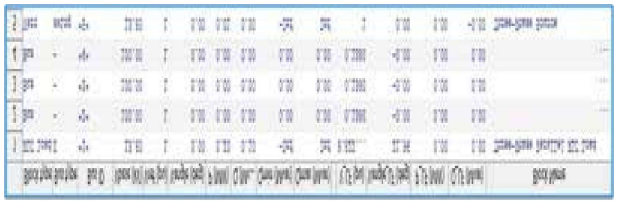

Fig. 13: Load flow report of the microgrid system with one DG connection for LLLG fault on line L1

Fig. 13 shows the load flow report table for the microgrid system with one DG connection for the LLLG fault that occurred on line L1. In this table, the load flow for one 3-phase source, one 3-phase RLC load, and three buses are shown.

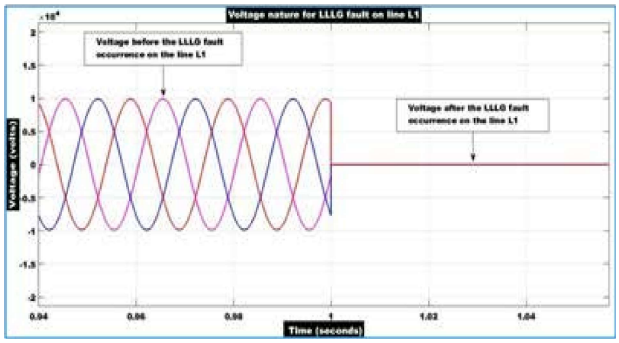

Fig. 14: Voltage nature for LLLG fault on line L1 before and after the fault

Fig. 14 illustrates the magnitude of the three-phase voltage for an LLLG fault on line L1, both before and after the fault, at a frequency of 50 Hz. During the usual working conditions of the microgrid system, the 3-phase voltage exhibits a sinusoidal waveform ranging from 0 to 1 second.

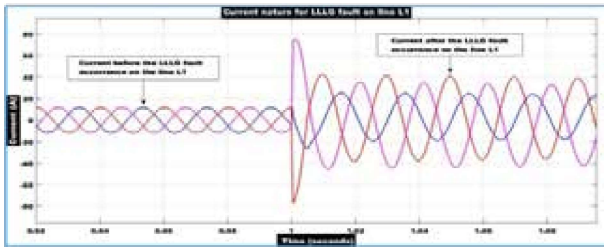

Fig 15: Current of LLLG fault on line L1 before and after the fault

The amplitude of this sinusoidal voltage before the fault event is 10 kV, ranging from 0 to 1 second, under normal operating conditions. However, when a three-phase short circuit line-to-line-to-ground fault occurs on line L1 at 1 second, the voltage of all three phases instantaneously drops to zero as a result of this LLLG failure on line L1. The voltage of these three phases remains at zero until the LLLG fault is completely resolved on line L1 in the microgrid system

Fig.15 illustrates the magnitude of the sinusoidal current in three phases for an LLLG fault on line L1, both before and after the fault has occurred, with a frequency of 50 Hz. During typical operation of the microgrid system, the 3-phase current exhibits a sinusoidal waveform with current magnitudes ranging from 10 to 15 A, during the time interval of 0 to 1 second. However, when a three-phase short circuit to line-to-line-to-ground fault occurs on line L1 at 1 second, the magnitudes of the currents in two phases increase instantaneously to 78 A, while the current in the remaining phase also increases instantaneously to 24 A due to the LLLG fault on line L1. The magnitude of the current will stay elevated until the LLLG fault on line L1 in the microgrid system is completely resolved.

Protection of AC Microgrid System from LLL-G Faults

In this section, we will examine the safeguarding of AC microgrid systems against three-phase SC LLLG failures in both grid-connected and islanded modes of operation. To study, analyze, and discuss the results, we examined this microgrid system in two specific case studies, referred to as Case Study - 1 and Case Study - 2. The load flow report of the microgrid system is obtained independently for each case study in both modes of operation using the power GUI block. The time-domain simulations, including outcomes, are comprehensively presented and analyzed for each case study, encompassing both modes of operation. The intricate models of microgrid systems being examined in both operational modes are created using the MATLAB/Simulink software environment.

Case Study - 1: Protecting an AC microgrid system using a current differential relay protection scheme in the event of a three-phase single LLG fault occurring on line L1 in both modes of operation (protecting faults occurring within the protected zone of the microgrid structure, such as faults on feeders, lines, buses, etc.).

Case Study - 2 Protecting an AC microgrid system by implementing an adaptive overcurrent relay protection scheme.

Case Study 1: Current Differential Relays

As seen in Fig.16, a comprehensive model of the microgrid network operating in island mode is displayed.

The table in Fig.17 displays the load flow evaluation for the microgrid network in the islanded mode of functioning. This table provides the load flow estimate for each bus. The block name, block type, bus type, and bus ID of every part are specified here.

The voltage load flow is in pu, and the voltage load flow angle is measured in degrees. All load flow estimates for the islanded mode functionality are derived and obtained from the power Gui block of the microgrid system's architecture when it is run in islanded mode.

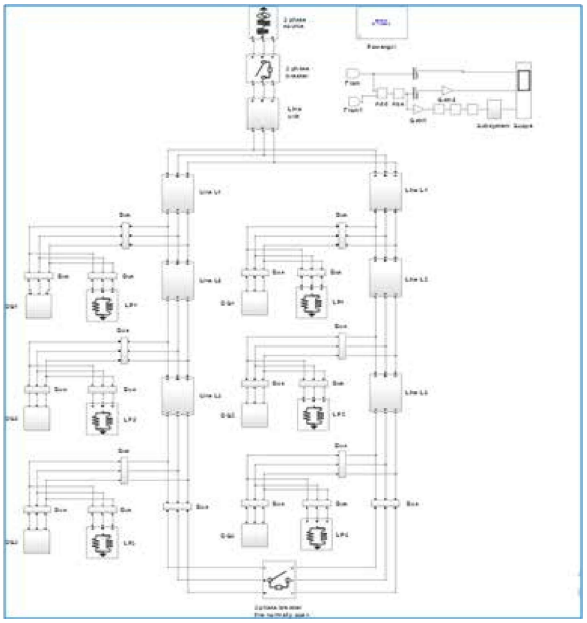

Fig. 16: Microgrid islanded mode of operation

Fig. 17: Load flow for an islanded mode of operation

Fig. 18 displays the outcomes of the microgrid system when functioning in islanded mode. A 3-phase LLLG defect is intentionally induced on the L1 phase of a 3-phase line, resulting in the display of 3 outcomes. The purpose of this is to safeguard both the consumers and equipment of the microgrid system from any 3 phase faults that may occur within the protected region. The existing differential relay protection technique effectively resolves these errors within a time frame of 0.1 to 0.2 seconds.During the disconnection of the microgrid system from the utility grid, the RBU1 current undergoes oscillations with a duration ranging from 0 to 0.1 seconds. During islanded mode, if line L1 fails, the current in RBU1 increases to 38 A for a single cycle. Following the resolution of the fault at 0.12 seconds on line L1, the current in RBU1 became stable and continued to flow steadily from 0.12 to 0.2 seconds.

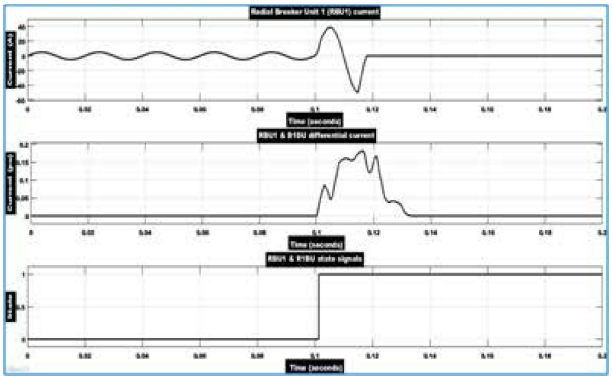

Fig. 18: Islanded mode of operation

In islanded mode, the differential current waveforms remain identical to those in grid-connected mode. The differential current waveform exhibits a rapid decrease in the current signal, and the relay encountered a peak current of 0.18 per unit (pu) between 0.1 and 0.13 seconds in islanded mode.

The differential relay successfully detected and resolved the line L1 fault in islanded mode within 0.1 and 0.14 seconds. Between 0.14 and 0.2 seconds, the differential current remains at zero until the finish.

• State signals of the Radial breaker unit 1 (RBU1) and the radial 1 breaker unit (R1BU).

This outcome demonstrates that the RBU1 and R1BU status signals in the islanded mode closely resemble those in the grid-connected mode.

Case Study 2: Adaptive Overcurrent Relays

Grid-connected mode.

Fig. 19 depicts the intricate model of the microgrid network operating in the grid-connected mode.

Fig. 20 displays the table that represents the load flow evaluation of a microgrid system in the grid-connected state of performance. This table provides the load flow estimations for each bus. Here, the block name, block type, bus type, and bus ID of each component are specified.

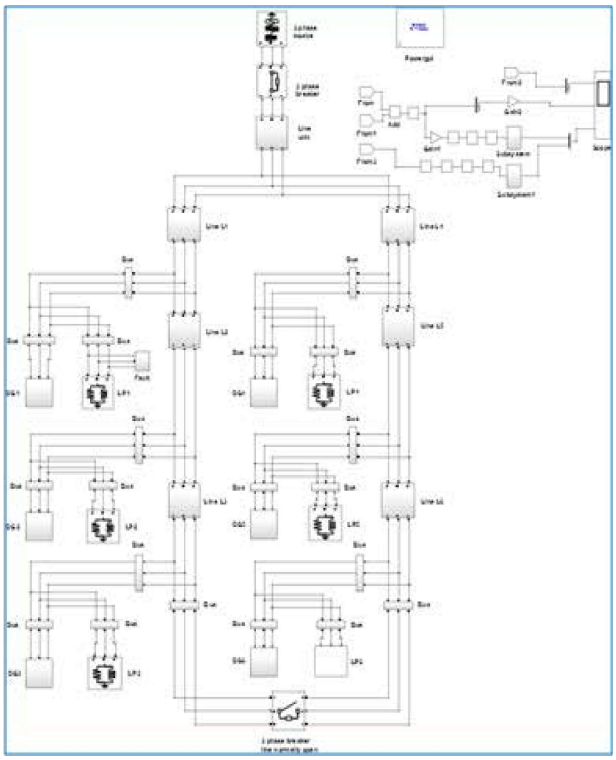

Fig. 19 Microgrid network operating in grid-connected mode

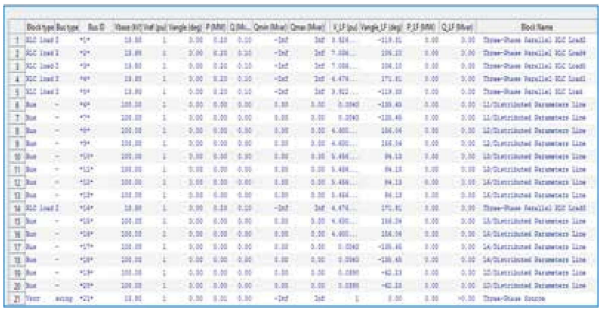

Fig. 20: Load flow for grid-connected mode

In the context of the microgrid system's grid-connected mode of operation, as depicted in Fig. 21, a comprehensive analysis of a 3-phase LLLG fault occurring at load point LP1 at 0.1 seconds reveals three key outcomes. This examination serves as a crucial aspect of safeguarding the microgrid system's consumers and equipment, offering protection against 3-phase faults that may arise beyond the designated protection zone (e.g., faults occurring at DGs, loads, etc.). The adaptive overcurrent relay protection scheme efficiently clears these faults within the timeframe of 0.1 to 0.2 seconds.

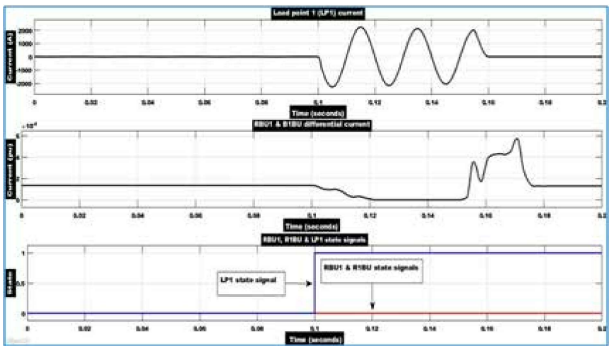

Fig. 21: Grid-connected mode of operation

The LP1 current initially flows consistently from zero up to 0.1 seconds. However, when a fault occurs at load LP1 at 0.1 seconds, the relay registers a substantial current spike, reaching up to 2220 A between 0.1 and 0.16 seconds. The adaptive overcurrent relay promptly operates and trips the respective circuit breaker after 0.1 seconds, successfully clearing the fault beyond the protection zone by 0.16 seconds. Subsequently, the LP1 current continues to flow consistently from 0.16 to 0.2 seconds, with the differential relay remaining inactive for faults occurring outside the zone of protection.

CONCLUSION

This paper concludes that this protection scheme for the microgrid system under the study operated effectively and protected the overall microgrid system from 3 phases of SC symmetrical LLLG faults are occurred in both grid-connected and islanded modes of operation. The current differential relay protection scheme operates successfully and protects the consumers as well as equipment connected to the microgrid system when 3-phase SC faults occur inside the zone of protection. Also, the adaptive overcurrent relays protection scheme operated successfully and protected the consumers as well as equipment connected in the microgrid system.

Also, this microgrid protection scheme shows feasibility and effectiveness in both modes of operation under the changing SC fault current level and varying fault impedance in the microgrid system. This protection scheme can be effectively implemented for symmetrical faults like LLL, and LLLG faults. This protection scheme improves the reliability, power quality, efficiency, and safety operation of both consumers as well as equipment connected to the microgrid system by clearing the 3-phase SC faults in the minimum possible time and by protecting the overall microgrid system effectively.

REFERENCE

1. F. Coffele, C. Booth, and A. Dysko, "An adaptive overcurrent protection scheme for distribution networks," IEEE Transactions on Power Delivery, vol. 30, April 2015.
2. S. Dambhare, S. A. Soman, and M. C. Chandorkar, "Current differential protection of transmission line using the moving window averaging technique," IEEE Transactions on Power Delivery, vol. 25, no. 2, April 2010.
3. N. Jayawarna, N. Jenkins, M. Barnes, M. Lorentzou, S. Papthanassiou, and N. Hatziagyriou, "Safety analysis of a microgrid," in 2005 International Conference on Future Power Systems, Nov 2005.
4. H. Nikkhajoei and R. H. Lasseter, "Microgrid protection," in 2007 IEEE Power Engineering Society General Meeting, June 2007.
5. I.Waseem, M. Pipattanasomporn, and S. Rahman, "Reliability benefits of distributed generation as a

backup source," in 2009 IEEE Power Energy Society General Meeting, July 2009.

6. N. A. Mohamed and M. M. A. Salama, "A review on the proposed solutions to microgrid protection problems," in 2016 IEEE Canadian Conference on Electrical and Computer Engineering (CCECE), May 2016.
7. M. Dewadasa, A. Ghosh, and G. Ledwich, "Protection of microgrids using differential relays," in AUPEC 2011, Sep. 2011.
8. H. Sonawane and M. Thakre, "Modified Distance Protection for Series Compensated (SC) Overhead Lines," 2021 Third Int. Conf. on Intelligent Communication Technologies and Virtual Mobile Networks (ICICV), 2021, pp. 468-474, doi: 10.1109/ICICV50876.2021.9388506.
9. F. C. Souza and B. A. Souza, "Adaptive overcurrent adjustment settings: A case study using RTDS," in 2013 IEEE PES Conference on Innovative Smart Grid Technologies (ISGT Latin America), April 2013.
10. R. M. Cheney, J. T. Thorne, and G. Hataway, "Distribution single-phase tripping and reclosing: Overcoming obstacles with programmable recloser controls," in 2009 Power Systems Conference, March 2009.
11. Kumar, N. Evaluation and Control Perceptive of VSM-Based Multilevel PV-STATCOM for Distributed Energy System. MAPAN 36, 561–578 (2021). https://doi.org/10.1007/s12647-021-00481-x
12. "IEEE application guide for IEEE std 1547(tm), IEEE standard for interconnecting distributed resources with electric power systems," IEEE Std 1547.2-2008, April 2009.
13. Z. Li, W. Tong, F. Li, and S. Feng, "Study on adaptive protection system of power supply and distribution line," in 2006 International Conference on Power System Technology, Oct 2006.
14. Vijay S. Kale, "An adaptive approach for three-zone operation of digital distance relay with Static Var Compensator using PMU," Int. Journal of Ele. Power & Energy Systems, Vol. 77, 2016, pp. 327-336, SSN 0142-0615, https://doi.org/10.1016/j.ijepes.2015.11.049.
15. D. Salomonsson, L. Soder, and A. Sannino, "Protection of low-voltage DC micro-grids," IEEE Transactions on Power Delivery, vol. 24, no. 3, July 2009.
16. A. Gururani, S. R. Mohanty, and J. C. Mohanta, "Microgrid protection using hilbert-huang transform based-differential scheme," IET Generation, Transmission Distribution, vol. 10, no. 15, 2016.
17. Ahmad, A. Interline Power Flow Controller (IPFC) Deployment in Long Transmission Lines and its Effects on Distance Relay. J. Inst. Eng. India Ser. B 103, 491–505 (2022). https://doi.org/10.1007/s40031-021-00637-y
18. S. Kar and S. R. Samantaray, "Time-frequency transform-based differential scheme for microgrid protection," IET Generation, Transmission Distribution, vol. 8, no. 2, February 2014.
19. P. R. Khade and M. P. Thakre, "Optimal Reach Settings of Mho Relay for Series Compensated Transmission Line Protection," 2020 4th Int. Conf. on Electronics, Communication and Aerospace Technology (ICECA), 2020, pp. 307-313, doi: 10.1109/ICECA49313.2020.9297516.
20. N. P. Matale, "Alleviation of Voltage Sag-Swell by DVR Based on SVPWM Technique," 2020 Int. Conf. on Power, Energy, Control and Transmission Systems (ICPECTS), 2020, pp. 1-6, doi: 10.1109/ICPECTS49113.2020.9336972.
21. M. Baran and I. El-Markabi, "Adaptive over current protection for distribution feeders with distributed generators," in IEEE PES Power Systems Conference and Exposition, 2004., Oct 2004.
22. S. Ganesan, "Selection of current transformers and wire sizing in substations," in 59th Annual Conference for Protective Relay Engineers, 2006., April 2006

Improving the Energy Efficiency of HVDC Grids by Implementing Approaches to Current Flow Control

Mohan Thakre, Ranjana Khandebharad
Sagar Kawade
SVERI' s College of Engineering
Pandharpur, Maharashtra
✉ mohanthakre@gmail.com

Archana Pawar
K.K. Wagh Institute of Engg, Education and Research
Nashik, Maharashtra

ABSTRACT

The escalating global demand for energy and the widespread integration of RES have reshaped the requisites of modern electricity grids. Modern grids must change to accommodate the transition to sustainable energy systems. HVDC technology emerges as a key facilitator for this transformation, offering advantages over traditional AC systems. However, the absence of strong and dependable safety mechanisms for DC fault clearance poses a significant obstacle to the implementation of HVDC grids.

The primary challenge associated with the VSC-HVDC system is the vulnerability to SC faults, which can result in damage to both the converter valves and the line network. Additionally, the existing DC breakers suffer from prolonged fault-clearing times, rendering them insufficiently fast and reliable for providing adequate protection on multi-terminal networks. To overcome these challenges, the integration of CFCs with a hybrid DC circuit breaker proves essential. This innovative approach aims to enhance the overall performance and resilience of the HVDC system, ensuring effective management of power flows and robust protection against DC faults.

KEYWORDS *: VSC, DC circuit protector, CFCs, HVDC grid.*

INTRODUCTION

HVDC systems have developed quickly in the past several years, and the number of HVDC projects worldwide has significantly increased. This increase is indicative of a resurgence of interest in VSC-HVDC technology. Concurrently, the effectiveness of MT-HVDC networks is growing increasingly when considering future power systems. It is anticipated that the networks will make it easier for electricity grids to incorporate large-scale renewable energy generation, allowing for cross-border energy trade. Currently, two MT-VSC-HVDC systems are operational: the 3-terminal Nano HVDC system and the five-terminal Zhou Shan network. Additionally, various alternative DC grid configurations have been recommended to outline the potential architecture of an upcoming European grid Meshed HVDC (MHVDC) networks face difficulties in managing power flows in addition to protection concerns, especially when they take on the intricate structure of MT-HVDC grids [6] [7]. Furthermore, there are several ways for current to flow between various nodes. CFCs are integrated with DCCB to address these issues.

CFCs are essential in meshed grids to prevent cable currents from overloading. In a meshed circuit, there are two main approaches to control current flow: modifying branch resistances and introducing a voltage source. Among various topologies, CFCs relying on de-de converters offer superior flexibility without the requirement for isolation transformers, distinguishing them from AC converter conversions. DCCB, on the other hand, functions when the power electronics path permits mechanical breakers to swiftly interrupt the DC and are crucial for protection against DC failures.

Fault protection and CFC functions can be combined into one cohesive system, as they currently exist as distinct functions. The coordination of CFCs in the design of a hybrid DC circuit breaker is examined in this work, with an emphasis on PHCBs (Proactive Hybrid

Circuit Breakers), particularly those that incorporate a load commutation switch (LCS). Power electronics components need to remain consistently linked to the DC power-carrying line for the proper functioning of the hybrid DCCB and CFC. The configuration of the converter (de-de), comprising two half-bridge converters connected to capacitors, with each half-bridge in series with the DC line, dictates the control and functioning of CFCs. Subsequently, a detailed examination of integrating DCCBs into CFCs is presented, offering insights into the two systems under investigation in this study.

THE PHYSICAL HYBRID CIRCUIT BREAKER (PHCB)

The primary, secondary, and energy-absorption branches make up the PHCB. The main branch has a mechanical switch (UFO) and a small set of semiconductor switches called the LCS. The secondary branch, on the other hand, has a considerable selection of semiconductor switches [1] [2]. The secondary branch, which is in charge of current-limiting functions in this architecture, is closely linked with the energy absorption branch.

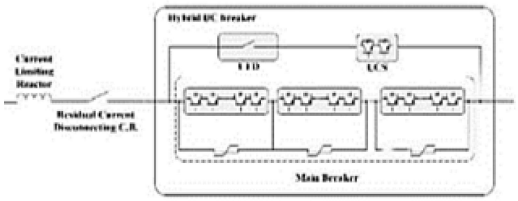

Fig. 1 PHCB

An essential part of the PHCB is the LCS, which diverts current from the mechanical switch and directs it into a circuit breaker that resembles a semiconductor [3]. Fig. 1 [13] analyzes and shows how to use and regulate this circuit breaker; further, more precise information is provided in [14] The concept of operation of the PHCB is illustrated in Fig. 1. Figure 2(a). When the current rises by 20% above the standard threshold, the system goes into fault case mode. The turn-off signal for the LCS is then recommended after a specific period. The current flow across the LCS during a transient fault is depicted in Fig. 2(b). [16]. Furthermore, research has been done on the design of alternative circuit breakers that are made up of comparable switches or LCSs [17-18].

Operation of PHCB

Fig. 2 depicts the PHCB working principle. As shown in Fig. 2(a), the IL normally travels via the UFD & the LCS. When the current is above the standard threshold by 20%, the system enters fault case mode. The LCS's turn-off signal is then suggested following a predetermined amount of time. The current flow during a short-lived fault across the LCS is as seen in Fig. 2(b).

The UFD disengages the LCS on one side and reroutes the current to the main breaker path immediately upon the LCS tripping. At this point, the current can be disconnected from the fault current using the main breaker [8–9]. Fig. 2(c) shows the current flowing via the route of the primary breaker. Lastly, the arrester linked in parallel across the main breaker dissipates the energy produced during the fault, as seen in Fig. 2(d).

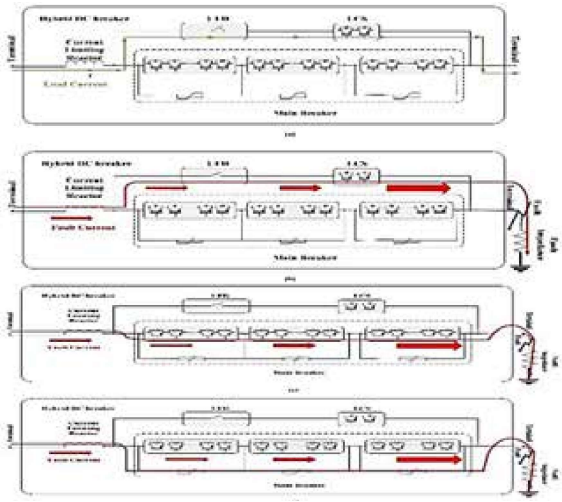

Fig.2 Protective HCB Operational

To reduce the amount of current that flows through the lines during faults, a reactor is connected in series with the main breaker and LCS.

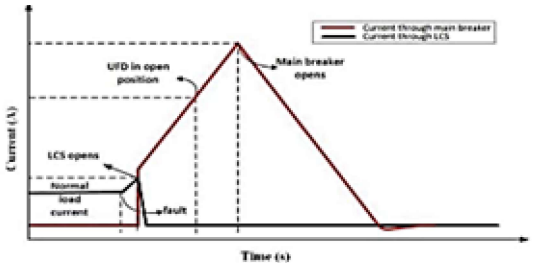

Fig. 3 I Control sequence of Proactive HCB

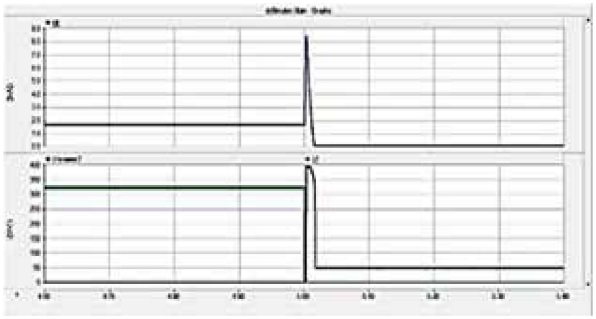

Fig. 4 Proactive HCB I and V O/p

Fig. 5 PHCB MB o/p

Fig. 3 [19] shows how the PHCB's control current flows. Fig 4 displays the PHCB's output voltage and current at 1.8 kA and 320 kV, respectively, while Fig. 5 displays the PHCB's MB output.

CURRENT FLOW CONTROLLER (CFC)

Fig. 6 shows the CFC diagram. The CFC is composed of eight different IGBT switches. A description of the CFC topology used in this work may be found in [12]. In essence, the CFC creates different voltage sources and keeps the line from overloading by removing power from one line to other. By circulating the DC along the lines of the HVDC grid, this process efficiently modifies the DC.

Table 1. Alternate CFC States

Mode	Higher Current	Current Direction	Switching States							
			Sa1	Sa2	Sb1	Sb2	Sc1	Sc2	Sd1	Sd2
1	I1	Forward	0	0	0	1	PWM	PWM	0	0
2	I2	Forward	0	0	1	0	PWM	PWM	0	0
3	I3	Reverse	PWM	PWM	0	0	0	0	0	1
4	I4	Reverse	PWM	PWM	0	0	0	0	1	0

In table I the input current is shown as "i," and the 2 branch currents are shown as "i" and "i z," that is, i, i", i z > 0. There are 4 modes of operation available to the CFC as it only regulates two wires (currents). First, two forward modes occur when currents flow out of the CFC in a forward direction, and two reverse modes occur when currents flow into the CFC in a reverse direction, where "0" indicates that the switch is in the off position and "1" indicates that the switch is on.

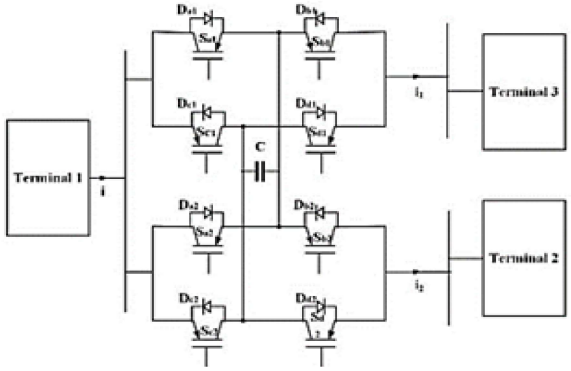

Fig.6. H-Bridge Dual CFC Topology

Computational Modeling of CFC

The CFC is capable of efficiently controlling cable current by combining certain switch states from Table I [20]. When handling overload problems, this functionality comes in handy because the CFC can switch the current from one line to another. The greater line current is used to charge the capacitor in the first mode of CFC operation, as shown by the following set of equations.

$$V = R_1 i_1 + L1L_1 \frac{di}{dt} + v_c + V_1 \quad (1)$$

$$\mathrm{V} = R_2 i_2 + L_2 \frac{\mathrm{d}i_2}{\mathrm{dt}} + V_2 \quad (2)$$

$$i1 = C \frac{dv_c}{dt} \quad (3)$$

By defining x, = [il iz vc] ' The aforementioned equations (1) through (3) can be classified in matrix form as where "T" denotes the transposition operation.

$$\begin{bmatrix} L_1 & 0 & 0 \\ 0 & L_2 & 0 \\ 0 & 0 & C \end{bmatrix} \frac{d}{dt} \begin{bmatrix} i_1 \\ i_2 \\ v_c \end{bmatrix} = \begin{bmatrix} -R_1 & 0 & -1 \\ 0 & -R_2 & 0 \\ 0 & 0 & 0 \end{bmatrix} \begin{bmatrix} i_1 \\ i_2 \\ v_c \end{bmatrix} + \begin{bmatrix} 1 & -1 & 0 \\ 0 & 0 & -1 \\ 0 & 0 & 0 \end{bmatrix} \begin{bmatrix} V \\ V_1 \\ V_2 \end{bmatrix} \quad (4)$$

Where, V is the bus voltage to which the CFCs is connected, V_z is the voltage at the terminal ends of the 1st and 2nd lines, and V_c is the capacitor voltage. L" RI and L_z' IS, respectively, stand for the first and second cables' series inductance and resistance.

In this way, the equations are given for the mode I capacitor discharge time, which occurs when the capacitor discharges from the lower line current i_z'.

$$V = R_1 i_1 + L1L_1 \frac{di}{dt} + V_1 \quad (5)$$

$$V = R_2 i_2 + L_2 \frac{di_2}{dt} - v_c + V_2 \quad (6)$$

$$i1 = -C \frac{dv_c}{dt} \quad (7)$$

Equations (5), (6), and (7) can therefore be rearranged as follows:

$$\begin{bmatrix} L_1 & 0 & 0 \\ 0 & L_2 & 0 \\ 0 & 0 & C \end{bmatrix} \frac{d}{dt} \begin{bmatrix} i_1 \\ i_2 \\ v_c \end{bmatrix} = \begin{bmatrix} -R_1 & 0 & 0 \\ 0 & -R_2 & 0 \\ 0 & -1 & 0 \end{bmatrix} \begin{bmatrix} i_1 \\ i_2 \\ v_c \end{bmatrix} + \begin{bmatrix} 1 & -1 & 0 \\ 0 & 0 & -1 \\ 0 & 0 & 0 \end{bmatrix} \begin{bmatrix} V \\ V_1 \\ V_2 \end{bmatrix} \quad (8)$$

The average model for CFC during i, > i z is obtained by multiplying equations (4) and (8) by (I-D) and D. The following equation is the result of combining this result with the charging mode of operation's duty ratio.

$$\begin{bmatrix} L_1 & 0 & 0 \\ 0 & L_2 & 0 \\ 0 & 0 & C \end{bmatrix} \frac{d}{dt} \begin{bmatrix} i_1 \\ i_2 \\ v_c \end{bmatrix} = \begin{bmatrix} -R_1 & 0 & -D \\ 0 & -R_2 & 1-D \\ D & -1+D & 0 \end{bmatrix} \begin{bmatrix} i_1 \\ i_2 \\ v_c \end{bmatrix} + \begin{bmatrix} 1 & -1 & 0 \\ 1 & 0 & -1 \\ 0 & 0 & 0 \end{bmatrix} \begin{bmatrix} V \\ V_1 \\ V_2 \end{bmatrix} \quad (8)$$

B=D* BI + (I -D) * Bz and A=D* Al +(I -D)* Az. The following is the form of equation (9) under steady-state conditions.

$$\begin{bmatrix} -R_1 & 0 & -1 \\ 0 & -R_2 & 0 \\ 0 & 0 & 0 \end{bmatrix} \begin{bmatrix} i_1 \\ i_2 \\ v_c \end{bmatrix} + \begin{bmatrix} 1 & -1 & 0 \\ 0 & 0 & -1 \\ 0 & 0 & 0 \end{bmatrix} \begin{bmatrix} V \\ V_1 \\ V_2 \end{bmatrix} = 0 \quad (10)$$

By solving equation (10), the stable-state value for the Vc can be expressed as:

$$V_c = \frac{\frac{R_2}{R_1} D(V-V1) + (V2-V)(1-D)}{\frac{R_2}{R_1} D^2 + (1-D)^2} \quad (11)$$

SYSTEM OVERVIEW AND MODELING FRAMEWORK

A single VSC powers each of the four stations that make up the M-HVDC grid. The stations are connected by four cables. A hybrid- CB is placed at each line termination, as shown in Fig. 7, and a CFC is addressed at Station 1. Two direct current CBs help the CFC coordinate its operations.

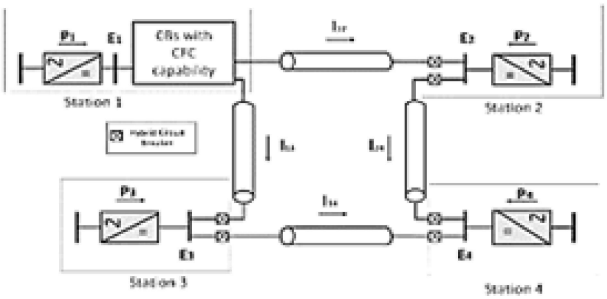

Fig. 7. One line diagram of Combined CFC and CBs

Computation of voltage source converter-based HVDC

Fig. 8 shows a four-terminal VSC-HVDC network made up of capacitors, a DC chopper, a DC inductor (DE), a PHCB, and high-pass filters that operate at 200 kV. In this setup, the rectifier and inverter use three-level NPC-VSC devices and neighboring IGBT/Diodes. Two 100 km lines and two 8 ml-l smoothing reactors are needed to combine the rectifier and inverter [5-6].

Even though the VSC-HVDC sector is currently seeing a rise in the use of CFC, three-level converters are still the preferred choice for many authorized projects. Thus, it is critical to take into account important interactions since the integration of CFC and the three-level composition may be crucial for future multi-Terminal direct current (MT-dc) grids. The midpoints of each

three-level converter are grounded by this MT system's grounding setup.

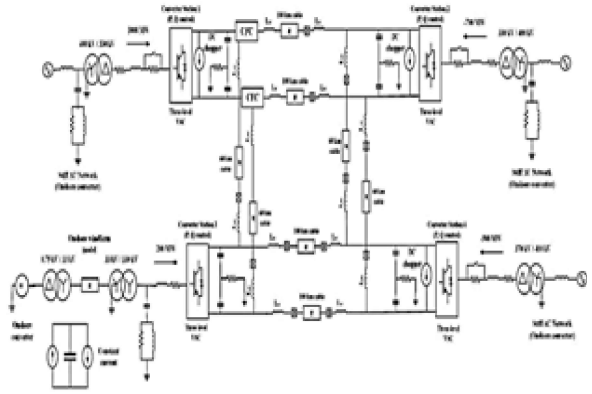

Fig. 8. Diagrammatic presentation of MT- VSC HVDC system

The three-level NPC design is built using phase reactors, transformers, switching IGBTs (insulated gate bipolar transistors), and capacitors (dc). The VSC-HVDC-MT system utilizes multiple control strategies, including voltage margin control and voltage droop [21] as shown in Fig 8. However, the P-Q control approach is utilized in this particular three-level model.

A number of DC choppers have been used in comparable configurations [23], and Table 2 contains an extensive list of them. The parameters related to the circuit breaker are also included in Table 3. The fundamental formulas that regulate the movement of both active and reactive power in a VSC-HVDC system are outlined below:

$$P = \frac{V_s V_c}{X} \sin \delta \qquad (12)$$

$$Q = \frac{V_s(V_s - V_c \cos \delta)}{X} \qquad (13)$$

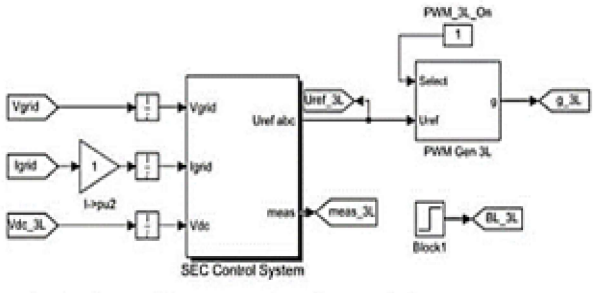

Fig. 9 System of Control at the Sending End Conversion

Equations (12) and (13) show that it is possible to regulate the two converter voltages' amplitudes to change reactive power, and to change the phase angle of the two converter voltages to control active power. When the converter's voltage Vc is at a greater angle than the source voltage (θS), it acts as a rectifier; otherwise, it acts as an inverter.

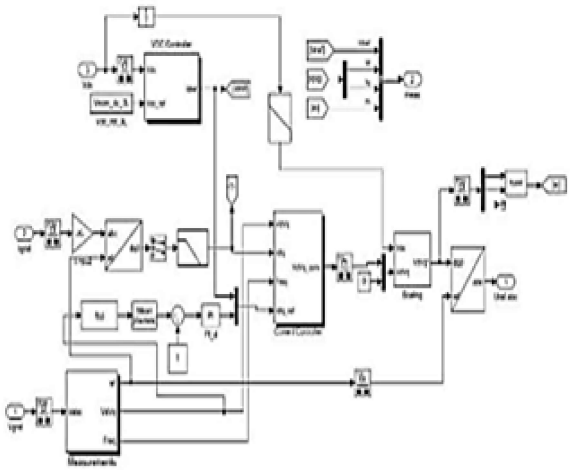

Fig. 10. Sending End Converter Control subsystem

Figures 9 and 10 depict the SEC's control system and subsystem. A current controller and three-level PWM are used to manage the rectifier side converter stations. Fig. 11 provides more information about the PLL, initializing filters, P-Q control, and the REC control system. All of these parts work together to guarantee the inverter side converter stations run smoothly.

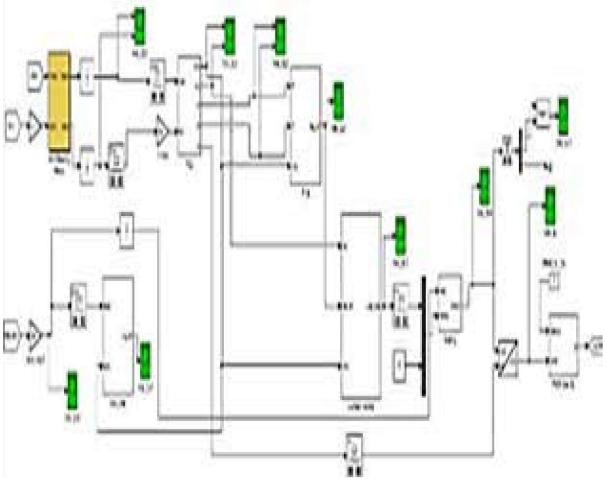

Fig. 11. Converter's Receiving End Control System

Table: 2 V & I Connection of DC chopper

Voltage (per unit)	Current (kA)
1	0
1.01	0
1.02	0.5
1.03	1
1.05	1.25
1.15	1.25

Table 3 Specification of CB

Parameters	Values
Stray Inductance (L1/Ls)	30 H
LCS snubber capacitance	5.5 F
LCS varistors knee voltage rating	7.92 kV
Main breaker snubber capacitor	0234 F
Main breaker knee voltage rating	320 kV
DC-line inductor	100 mH
Mech. Operating time	2 ms

SIMULATION OUTCOMES AND ANALYSIS

Fig. 12 displays the direct-axis reference current at 1.5 per unit along with the direct and quadrature-axis current at the SEC. Potential conflicts within the systems are shown by the Q and Q output at the REC that is shown in Fig. 13.

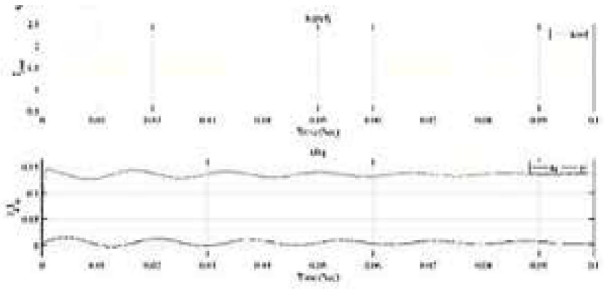

Fig. 12 d, q-axis Sending End CS current.

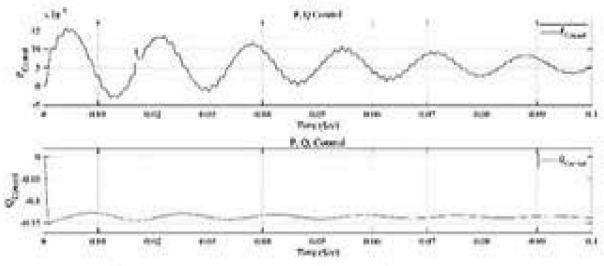

Fig.13 P, Q o/p at Receiving End CS

The response of the designed control system was evaluated by simulating the system depicted in Fig. 8 through the use of MATLAB SIMULINK software. Three-level NPC-VSC was employed for the entire simulation. The VSC-HVDC system effectively manages the flow of both active and reactive power, along with AC voltage regulation, as long as the load constitutes an active AC system. Two significant studies discuss the operation of PHCB, with or without CFC coordination support.

Study 1

Study 1 shows that in a four-terminal VSC-HVDC system, the second and fourth converters work as inverters to maintain DC voltage, while the first and third converters act as rectifiers to maintain P and Q power. The rectifier side's three-phase voltage and current are examined in Fig. 14. P and Q power parameters are both fixed at 0.17 watts per unit. The study's findings are shown in Fig. 15, 16, and 17, in that order.

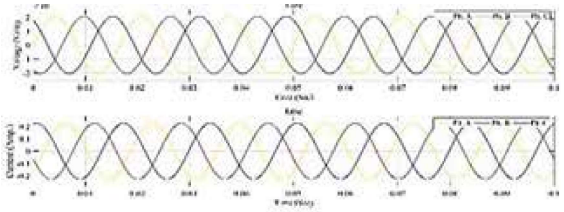

Fig. 14 3-ϕ Alternating V & I

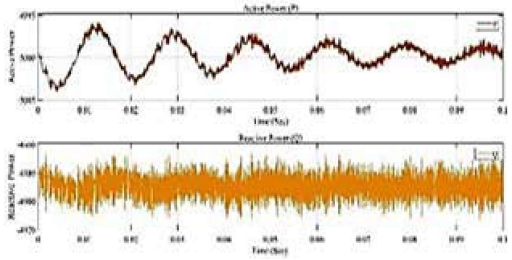

Fig 15. P and Q Power

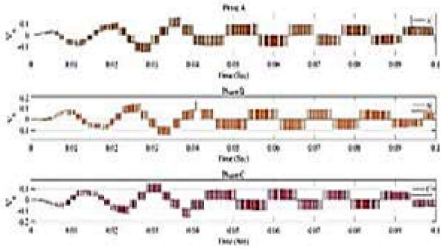

Fig. 16 I/p Signal for 3-level VSC

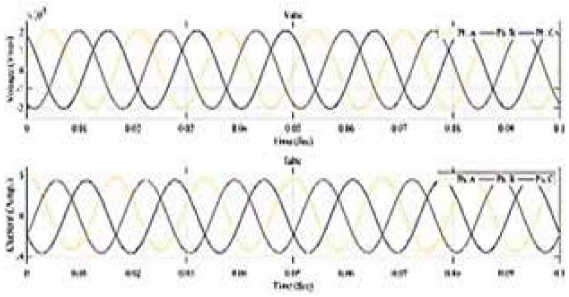

Fig. 17. 3-ϕ V-I Measurement

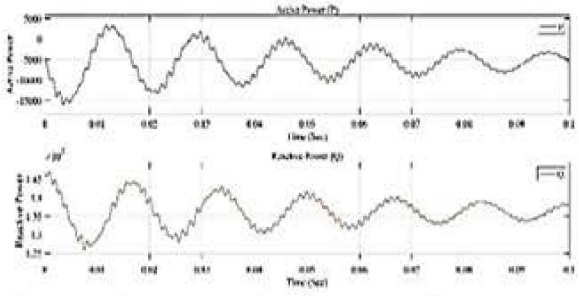

Fig. 18. P & Q at Supply Terminal

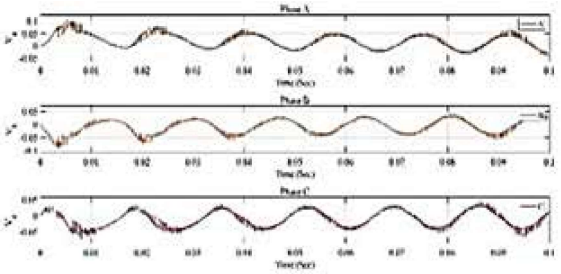

Fig.19. I/p Signal at 3-level VSC

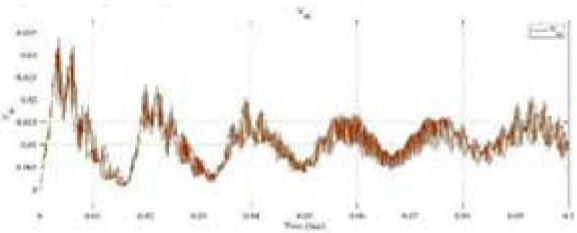

Fig. 20. O/p Signal at 3-level VSC

CONCLUSION

There are many benefits to integrating CFC with hybrid circuit breaker designs. A four-terminal VSC grid with a two-independent-converter architecture has been used to validate this notion. To minimize overall grid power losses or avoid overloading separate conductors, the CFC actively regulates the current inside the DC grid. In addition, the controller can oversee other grid functions like line switching and perhaps reduce the number of switching devices. The findings show that fewer space requirements and power losses occur from the CFC and circuit breaker working together. Additionally, the DC circuit breaker shields the CFC from overvoltage. The breaker's action diverts current away from the CFC during transient DC fault currents. When compared to independent systems, this voltage reduction permits a depletion of power losses in the combined case studies.

REFERENCE

1. Q. Guo, M. Yoon, J. Park, and G. Jang, "N ovel topology of current interruption and de circuit breaker in hvdc networks," IEEJ Transactions on Electronic and Electrical Engineering, Feb 2017.
2. S. Wang, C. Li, O. D. Adeuyi, G. Li, C. E. Ugalde-Loo, and J. Liang, "Coordination of mmcs with hybrid dc circuit breaker s for hvdc grid protection," IEEE Transactions on Power Delivery, vol. 34, no. I, pp. 11-22, Feb2019
3. H. Rao, "Architecture of nano multi-terminal vsc-hvd c system and its multi-functional control," CSEE Journal of Power and Energy Systems, vol. I, pp. 9- 18, Mar ch 201 5.
4. L. Zhen-dong, T. Yu-don g, Z. Zhe-yuan, W. Xiao-bo, F. Cai-jie, L. Li, and H. Van, "The parameters and model based on the operation mode of a multi-terminal 500 kv flexible e de power grid," International Journal of Engineering Thermos physics and Power Engineering (2017), vol. I, pp. 16- 24.
5. W. Xiao, M. S. EI Moursi, and A. Moawwad, "A novel transient control strategy for vsc-hvdc connecting offshore wind power plant," IEEE Transactions on Sustainable Energy, vol. 5, no. 4, pp. 1056- 1069, Oct 2014
6. O. Ruiton, N. M. MacLeod, J. D. Whe eler, F. Ga loon, and D. Ingemansson, "The south west scheme: A new hvdc and hvac transmission system in sweden," 10th lET International Conference on AC and DC Power Transmission (ACDC 2012), pp. 1- 5, Dec 20 12.
7. G. Bu igues, V. Valverde, A. Etxegara i, P. Eguia, and E. Torres, " Present and future multiterminal hvdc systems: current status and forthcoming," Renewable Energy and Power Quality Journal, vol. I, pp. 83-88,

Apr il 20 17.

8. O. Cwikow ski, 1. Sau-Bassols, B. Chang, E. Prieto-Araujo, M. Barnes, Q. Mu, J. Liang, Y. Li, and X. Zhou, " Power flow control dev ices in de grids," IEEE Power and Energy Society General Meeting, pp. 1-7, July 2012.
9. O. Bellmunt , and R. Shutt leworth, " Integrated hvdc circuit breakers with current flow control capability," IEEE Transactions on Power Delivery, vol. 33, pp. 1-10, June 2017.
10. B. Ooi and E. Veilleu x, "Thyristor power-flow controller with multi terminal hvdc," IEEE Transactions on Power Delivery; vol. 27, no. 3, pp. 1205- 1212, July 2012.
11. R. S. Whitehouse and C. D. Barker, "A current flow controller for use in hvd c grids," pp. 1- 5, De c 20 12.
12. K. Muriuki, C. M. Muriithi, L. Ngoo, and G. Nya koe, "Review of hvdc circuit breakers topologie s," IOSR Journal of Electrical and Electronics Engineering (IOSR-JEEE), vol. 12, pp. 109-117, MayJune 2017.
13. H. B. J. M. Callavik, A. Blomberg, "The hybrid hvdc breaker," ABB Grid Systems, Technical Paper, pp. 1-10, Nov 2012.
14. O. Cwikowski, M. Barnes, R. Shuttleworth, and B. Chang, "Analysis and simulation of the proactive hybrid circuit breaker," IEEE 11th International Conference on Power Electronics and Drive Systems, pp. 4-11, June 20 15.
15. A. Hassanpoor, J. Hfuer, and B. Jacobson, "Technical assessment of load commutation switch in hybrid hvdc breaker," IEEE Transactions on Power Electronics, vol. 30, no. 10, pp. 5393 -5400, Oct 2015.
16. O. Cwikowski, " Synthetic testing of hvdc cirucit breakers," Ph.D. dissertation, School Electr. Eng., Univ. Manchester, Manchester, u«, 2016.
17. W. Zhou and et a I., "Testing and development of a 200 kv full bridge-based hybrid hvdc-breaker," in Proc. 17th Eur. Corf. Power Electron. Appl., pp. 1- 7,20 15.
18. D. L. Penache and 1. P. Dupraz, " Development of a 120 kv decb," ClG RE, Paris, France, pp. 4- 301 ,20 14.
19. Hafner and B. Jacobson, "Proactive hybrid hvdc breakers- a key innovation for reliable hvdc grid," Cigre symposium, Bologna, Italy, pp. 13- 15, Sept. 2011.
20. O. G.-B. Sau-Bass ols and E. Prieto-Araujo, "Control and modelling of an interline cfc for meshed hvdc grids," IEEE Trans. Power Del., vol. 32, no. I,pp. 11-22 , Feb. 2017.
21. W. Wan g, M. Barnes, and O. Marjanovic, "Droop control modelling and ana lysis of multi-terminal vsc-hvdc for offshore wind farms," 10th IET International Conference on AC and DC Power Transmission (AC DC 2012), pp. 1- 6, Dec 2012.
22. T. M. Hailese lassie and K. Uhlen, " Impact of de line voltage drops on power flow of mtdc using droop control," IEEE Transactions on Power Systems, vol. 27, no. 3, pp. 144 1-1 449, Aug 2012.
23. S. K. Chaudhary and e. a. R. Teodores cu, P. Rodrigue z, " Modelling and simulation of vsc-hvdc connection for wind power plants," Proc. 5th Nordic Wind Power Conf, 2009
24. Gaidhani, T., & Thakre, M. P. (2020, December). HVDC fault current reduction through MMC and DCCB coordination. In 2020 International Conference on Power, Energy, Control and Transmission Systems (ICPECTS) (pp. 1-6). IEEE.
25. A. K. Kale and M. P. Thakre, "Integration of Proactive Hybrid Circuit Breaker with Current Flow Controller for Bipolar HVDC Grid," 2019 International Conference on Power Electronics Applications and Technology in Present Energy Scenario (PETPES), Mangalore, India, 2019.
26. Gaidhani, T. S.,. (2020, November). Analysis of MMC coordination with hybrid DC breakers for HVDC grid protection. In 2020 4th International Conference on Electronics, Communication and Aerospace Technology (ICECA) (pp. 333-338). IEEE.
27. Gaidhani, Tejas & Kale, Akshay. (2019). VSC-HVDC Bipolar Grid Based on Novel Distance Protection Scheme. International Journal of Recent Technology and Engineering (IJRTE).

Optimizing Automotive Performance: A Comprehensive Comparison of DC-DC Converters

Vinayak Gaikwad, Prerna Goswami
Institute of Chemical Technology
Mumbai, Maharashtra
✉ ele19vr.gaikwad@pg.ictmumbai.edu.in

Atharva Manurkar, Roshan Chaudhari
Honeywell Automation India. Ltd.
Pune, Maharashtra

Mohan Thakre
SVERI's CoE
Pandharpur, Maharashtra

ABSTRACT

To effectively manage power in line with Energy Management controller recommendations, a bidirectional DC/DC converter must be meticulously chosen for use in battery/ultracapacitor (UC) electric vehicle (EV) applications. After thoroughly comparing three-level DC/DC converters with traditional two-level and interleaved bidirectional buck/boost designs, this study firmly supports their use. We cover all the bases in our review, including the size or the weight of the magnetic components and their overall efficiency.

Unlike earlier comparative studies that rely on fixed input and output parameters, this method offers a new perspective by using power references from a wavelet transform based energy management strategy. This allows for a more accurate evaluation of the converter's performance in dynamic operational settings by accounting for fluctuations in the voltages of the energy sources and the traction power. Thorough evaluations reveal that the three-level converter is the best, exhibiting not just improved overall efficiency but also a smaller inductor. A meticulously designed proof-of-concept These results are supported by a 1-kW bidirectional three-level DC/DC converter, which achieves a remarkable peak efficiency of 93.2% at a switching frequency of 200 kHz. The three-level converter's innovative approach and convincing evidence make it a practical and effective choice for battery/UC EV power processing.

KEYWORDS *: EV, Interleaved converter, Ultracapacitor, Non-isolated dc to dc converter, Three level converters.*

INTRODUCTION

EVs with UCs can become attractive substitutes for battery-only models with large capacity batteries [1]. Based on factors like efficiency, control complexity, and performance, several drivetrain topologies with active or passive UC control are put forth and contrasted [2].

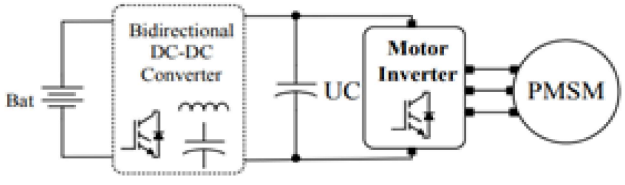

Fig. 1. The battery/UC vehicle's drive train features a converter

Fig. 1 illustrates the usual connection type, where the UC is directly linked to the dc link and functions as a power buffer. With the bidirectional dc to dc converter serving as the only controllable unit, UC must regulate the voltage within the top and lower operational limits of the inverter in order to meet high power needs.

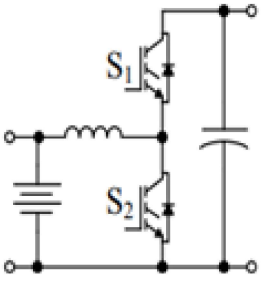

(a) 2-level (CBC)

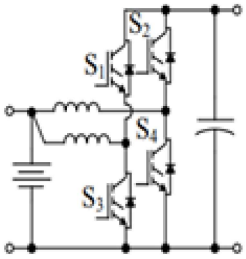

b) Interleaved (BIC)

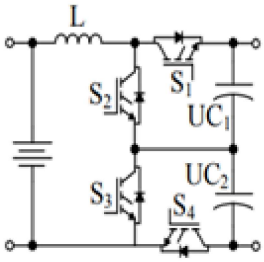

(c) 3-level (TLC).

Fig. 2. buck/boost converters

Due to it has a significant impact on the system performance overall, choosing a bidirectional converter hierarchy is essential.

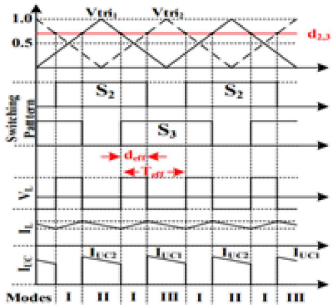

(a)d > 0.5

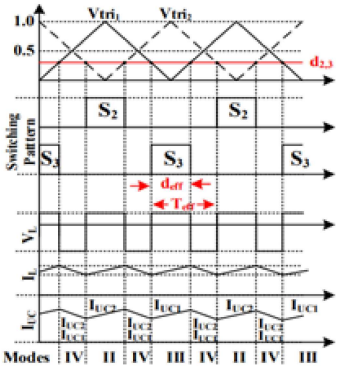

(b)d<0.5

Fig.3.Switchingscheme

Previous works have suggested and examined bidirectional dc to dc converters for EVs; the majority of these studies gives efficiency assessments for specific power circumstances with defined input and output characteristics [3]. A study of DC-to-DC converters in EVs. According to this study, the bidirectional dc/dc converter in EVs should be a 3-Level Converter (TLC). [4]. It compares this converter which are shown in Fig. 2 [5]. As the drive cycle, use the Urban Dynamometer Driving Schedule (UDDS).

Together with the appropriate UC and battery voltages, the power distribution which is calculated using 3-level Discrete Wavelet Transformation in [6] is employed in estimates of efficiency and magnetic parameter size.

In order to determine which converter has the highest efficiency and the smallest magnetic component size, efficiency models that have been developed are utilized to calculate the converters' overall efficiency over the course of the driving cycle. It is possible to extend this analytical pathway to additional applications, such as fuel-cell, PHEV [6]

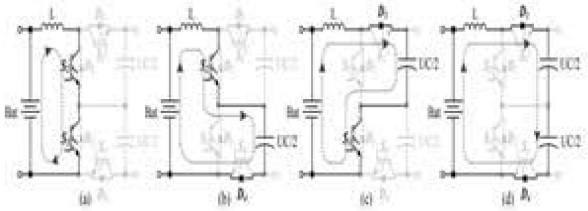

Fig. 4. Functionality of Boost mode

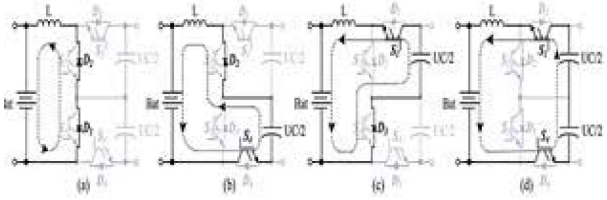

Fig. 5. Buck mode operation

On the other hand, the boost inductor in CBC becomes an important part in high-power applications, adding to the system's weight, volume, and cost. Higher losses are also a result of the requirement for high-voltage switches in CBC. Compared to the CBC, the use of a Three-Level Converter (TLC) is a viable substitute that offers significant advantages [7-8].

The TLC converter's switching architecture is displayed

in the Fig. 3. The phase-shifted switch turn-on periods result in a ripple frequency in the effective inductor current is twice that of usual designs [9].Fig. 4 and 5, respectively, show the boost and buck operation modes of the TLC. The boost mode is the one being explained, even though both modes do similar tasks. There are four distinct modes of circuit operation, and the corresponding circuits are classified according to the duty cycle value. The duty cycle's climax value, represented by the letter "d," is 0.5. The comparable circuit sequence repeats as IV-II-IV-III for d< 0.5. An control signal overlap happens as the duty cycle rises over 0.5, creating a new equivalent circuit sequence, I-II-I-III[10-11].

DIFFERENT ANALYSIS

Comparing TLC to the most sophisticated CBC and BIC converters reveals a number of advantages. The voltage across the switch controls a significant amount of the switching loss. Specifically, exposing the switches to half of the output voltage, even in the absence of soft-switching, can significantly lower the parasitic capacitance's switching loss as compared to CBC. Indeed, employing low voltage switches is expected to significantly reduce losses due to parasitic capacitance [12]. This section compares and contrasts the two different topologies for bidirectional buck/boost dc-dc converters shown in Fig. 2, accounting for the power handled by the converter as well as the dynamic fluctuations of the battery and UC voltages. The comparison is based on the size and efficiency of their magnetic components over the entire drive cycle range. Obtain Cycle A. Common Elements was established. The dynamic voltage changes of the energy sources and the load power have a significant impact on the efficiency of the bidirectional converter.

In the drive train architecture depicted in Fig. 1 the energy sources and batteries. Because the UDDS driving cycle simulates a 7.5-mile urban route with numerous pauses, it was used for this experiment [13]. When operating in a linear mode, the battery voltage can fluctuate between 350V and 380V. The UC's voltage is limited to 350V by the inverter's minimum working voltage, even though it is directly connected to the DC connection and so cannot exceed 600V. A voltage swing from 600V to 350V can be stored in the UC for a total energy of C•118.75kJ, where C is the capacitance of the UC. This is due to the fact that the UC's energy storage is exactly proportional to the voltage squared. [14].

Table 1. Currents of Conversion During Four UDDS

	CBC 200µH	TLC 100µH	BIC 200µH
Max. Bat. Cur. [A] (i_{bat_max})	138.64	130	123.2
Ripple Cur. @ i_{bat_max} [A]	30.86	4.28	15.43
Max. Ind. Cur. [A] (i_{L_max})	138.64	130	77.03
Ripple Cur. @ i_{L_max} [A]	30.86	4.28	30.86
Max. Ripple Cur. [A] (Δi_{bat})	32.94	11.5	15.8
Max. Ripple Cur. [A] (Δi_L)	32.94	11.5	31.6
Max. Ind. Rms Cur. [A]	126.89	126.86	63.49

In the current study, three-level wavelet decomposition was used to derive reference powers for the battery and UC [23].

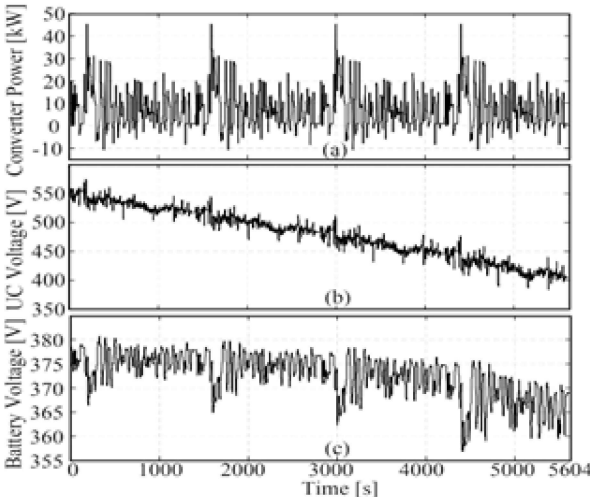

Fig. 6. Dynamic Fluctuation of state variables

Fig. 6 displays the battery, UC voltage fluctuations, and converter power throughout the course of four UDDS cycles. In this instance, we're assuming that the battery started off with a SOC of 80%.

In the sections that follow, size and efficiency studies will be carried out using this data. The scale of the magnetic component B. Peak flux density is inversely related to the size of the magnetic component and is determined by the peak current flowing through the core. This is how the battery's current ripple appears in CBC: [15-16].

$$\Delta_i bat_{boost(d)} = \frac{V_o}{Lf_s} d(1-d) \quad (1)$$

The TLC's battery current ripple is,

$$\Delta_i bat_{-TL}(d) = \frac{V_o}{2Lf_s} d_{eff}(1 - d_{eff}) \quad (2)$$

The relationship between the duty cycle of a switch in a transverse light-coupler (TLC) converter and the ripple current may obtained by altering the duty cycles that are effective from Eq. (1) & (2) and it became as shown in Eq. (3)[17].

$$\Delta_i bat_{-TL}(d) = \begin{cases} v_o \\ Lfs \end{cases} d(1 - d) \quad (3)$$

Two inductor currents added together make up the BIC converter's input current as shown in Eq.(4). If the switches duty cycles are below 50%, the input current ripple will develop into

$$\Delta_i bat_{-Interleaved}(d) = \frac{2V_{in} - v_o}{Lf_s}\left(1 - \frac{V_{in}}{V_o}\right) \quad (4)$$

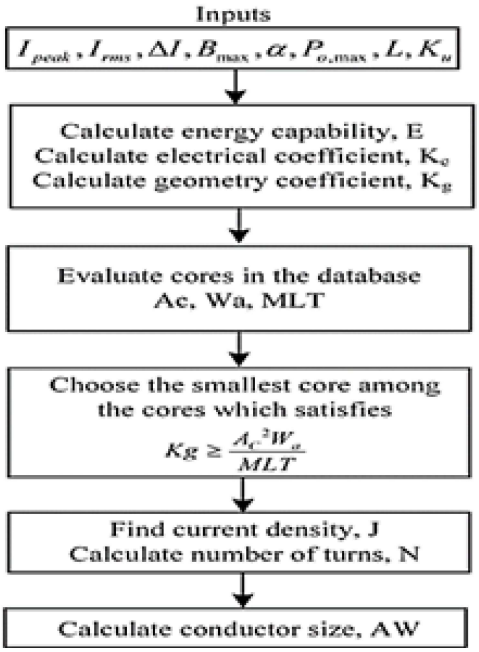

Fig. 7. Flow diagram for the core geometry estimation approach-based inductor design method

A ripple in the input current is defined as a situation where the duty cycle is over fifty percent. as refer in Eq. (5).

$$\Delta_i bat_{-Interleaved}(d) = \frac{V_o - 2v_{in}}{Lf_s}\left(\frac{V_{in}}{V_o}\right) \quad (5)$$

Assuming that Eq. (6) is satisfied for the current ripple of all interleaving inductors,

$$\Delta_i bat_{-Interleaved}(d) = \frac{v_o}{Lf_s} d(1 - d) \quad (6)$$

At 75% duty cycles, BIC and TLC reach the greatest input ripple current, while CBC reaches their highest at 50%. The inductance needed by CBC is four times greater than that of TLC for the same peak ripple in battery current.

The size of the magnetic core can be determined by measuring the extreme inductor current and necessary inductance. In light of this, the drive cycle depicted in Fig. 6 has been assessed using a switching transitional converter operating at a frequency of 20 kHz.

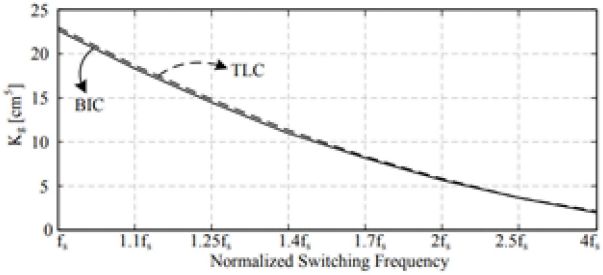

Fig.8. BIC and TLC core weights

Table 2Size of CBC, TLC, and BIC inductor

	CBC (200μH)	TLC (100μH)	BIC (200μHx2)
K_e	0.164	0.164	0.0853
K_g	170.1	42.5245	
J [A/cm^2]	263.2	263.2	336
N	38	38	42
AW [cm^2]	AWG#1/0	AWG#1	AWG#4
Wire	AWG#20	AWG#22	AWG20
	×105	×167	×49
W_a [cm^2]	46.8	46.8	24.41
A_c [cm^2]	13.56	6.78	7.16
Core	0077339A7	0077339A7	0077907A7
	×2	×1	×6
Weight [Kg]	1.3×2	1.3	0.262×6

However, 400μH produces a very big magnetic core, as will be discussed later. Thus, 200μH is chosen as the CBC's inductance [18-19]. Table1 shows that 138.7A, with a ripple of 32.9A, is the maximum current that may be taken from the battery in CBC. An inductor current ripple of 30.8A is used to get the maximum inductor current of 77A for BIC Even though this ripple has no effect on the battery itself, itlooks at how it impacts the core losses in the sections that follow.

Estimate the magnetic component's magnitude using the core geometry methodology. To estimate the core

size, various elements must be determined, such as the needed inductance (L), window utilization factor (Ku), maximum flux density (Bmax), regulation (α), peak current (Ipeak), rms current (Irms)and regulation (α) [20].

Table 3 Analyzed Converter Specifications

	CBC	TLC	BIC
Input Voltage [V]	357-381	357-381	357-381
Output Voltage [V]	384-575	384-575	384-575
Peak Prop. Power [kW]	45.32	45.32	45.32
Peak Regen. Power [kW]	-10.78	-10.78	-10.78
Power Switch	IXFB30 N120P	IXFX80 N60P3	IXFB30 N120P
Switch Ratings	1200V/30A	600V/80A	1200V/30A
No. of Switches	12	8	12
Swit. Freq. [kHz]	20	20	20
Ind. Ripple Freq. [kHz]	20	40	40
Inductance [μH]	200	100	200
No. of Cores	2	1	6
Cores Weight [kg]	2.6	1.3	1.6

This is influenced by the magnetic and electric factors.

$$E^2 = K_g . K_e . \propto \tag{7}$$

The electrical coefficient, denoted as E, can be calculated using the formula 0.5·L·Ipeak2, where L represents the magnetic quantity and Ipeak represents the electrical quantity shown in Eq. (8).

$$K_g = 0.145\, P_o B_{\max}^{-4} \tag{8}$$

The identification and evaluation of kg are essential components of the estimation approach. However, some of the core makers directly supply the Kg [cm5] value linked with every core. A mathematical representation of the relationship between area product and Kg is as follows with reference of Eq. (9):

$$K_g \geq \frac{A_c^2 W_a}{MLT} \tag{9}$$

The term mean length per turn, or MLT is used. The maximum flux density can be divided by the area to find the current density as in Eq. (10).

$$J = \frac{2.E.10^4}{B_{\max}.\, A_c\, W_a\, K_u} \tag{10}$$

The wire size is determined by the current density in Eq. (11).

$$J = \frac{I_{rms}}{J} \tag{11}$$

From Eq. (12), the total amount of turns could be determined by using the provided wire size as well as winding area.

$$N = \frac{W_a K_u}{A_w} \tag{12}$$

Fig. 7 shows the schematic of the choosing an inductor core process. What matters most is the core material you choose for the maximum flux density. The cores with distributed air gap having a saturation flux density of 1.1–1.5 T are known as magnetic or iron powder cores. These cores find their most common use in power inductors, more especially in DC inductors and the switched mode power supply (SMPS) output filters. Eq. (13) & (14) show that increasing the maximum operational flux decreases the area product of the core, an estimate of the core size; yet, increasing the core losses causes the area product to grow.

In this example, it is expected that the maximum flux density is roughly 0.5 T, which is the value commonly used as Bmax/2. The standard value of the fill factor Ku is 0.4. The control α is usually set at 1% in low power applications, but as power grows, it is frequently bounded to a lower level. The maximum power, 45.23kW, is reached before regulation is capped at 0.1%. The remaining parameters Ipeak, Irms, ΔI, L, and Po,max are necessary to determine the product area and, by extension, the core size. They are derived from the dynamic modeling of four UDDS drive cycles. For measuring core size, the kg is a helpful unit of measurement [21]. The calculated kilogram (Kg) values for TLC and BIC for different switching frequencies are shown in Fig. 8. Fig. 8 omits the CBC because its kilogram value is much greater. It clearly shows that Kg is somewhat greater for TLC converters, but else it is much the same for BIC converters. Please be aware that the BIC values include the total kilograms for two identical cores. Since commercially available cores do not always have the precise winding and cross-sectional areas predicted by Kg, the former is not always applicable to actual implementation. An iterative technique is utilized to generate approximate core sizes for Kool Mu (sendust core) cores based on the given requirements.

When compared to powdered iron cores, these cores are recognized for their much superior thermal

characteristics, reduced losses, and modest cost. Fig. 7 provides an illustration of the algorithm. The area product of this core type can reach up to 791 cm4 of the cores stored in the database, the algorithm chooses the most useful one. Table 2 presents the findings related to the basic design. The core weights of TLC, BIC, and CBC converters are respectively 1.3 kg, 0.662 kg, and 2*1.3 kg. Part C: Rules for Choosing Semiconductors It is important to evaluate the current and voltage pressures on the power switches before making a selection. Unlike TLC, where the switches are exposed to half of the output voltage, CBC and BIC expose the switches to the whole output voltage. The results of the calculations presented in previous section.

A Indicate that 575V Is the upper limit for ultra-capacitors. It follows that TLC switches should have ratings greater than 287V and CBC and BIC switches should have values greater than 575V. Furthermore, due to the hard-switched nature of the converters, the circuit's parasitic output capacitances and inductances may resonate, raising the peak voltage across the switches well above this threshold. Therefore, it is imperative to allocate a margin of safety. We can see that TLC needs 600V switches, but CBC and BIC need 1200V switches based on this value of 2. It can be shown from Table 1.

When considering these parameters, IGBTs stand out as possible semiconductor devices, while MOSFETs are more suited as switching devices for frequencies between 20 and 40 kHz. On the other hand, high current rating discrete MOSFETs with voltage ratings of 1200V or even 600V are not easy to come by. High power IGBT modules or parallel linked [22].

MOSFETs are the two options that are dictated by these restrictions. The feasibility of a parallel-connected MOSFET structure is determined by taking the switching frequency and switch cost into account. Since many manufacturers use different standards to sell their products, we choose 600V and 1200V MOSFETs from the same brand and category/family so that we can compare them fairly. Considering these factors, the 1200V/30A power MOSFETs IXFB30N120P and the 600V/80A IXFX80N60P3 were chosen for the TLC and two-level converters of CBC and BIC, respectively. Twelve IXFB30N120P MOSFETs are employed in the CBC and BIC converters collectively, and eight IXFX80N60P3 MOSFETs in the TLC [23].

PERFORMANCE ASSESSMENT

We design and analyze complete efficiency models that account for a range of losses, in order to assess the energy loss and overall converter efficiency during the driving cycle. 5605 data points are analyze for every converter in this thorough investigation utilizing the parameters indicated in Table 3.

Switching Losses

At frequencies higher than 20 kHz, power dissipation is caused by four main components of switching losses. These parts are described below:

Overlap Power Losses (VDS and ID) in MOSFETs

The switching instant is when the current and voltage bleed over, causing these losses. The region under the drain current (ID) as well as drain-source voltage (VDS) waveforms quantitatively depicts them.

Charge Loss at the Gate (Qt)

The charge that is discharged to the ground in each switching cycle from the gate capacitance, which is charged with gate voltage (VG), is the source of Qt. Due of this, it is considered a switching loss.

Capacitance Losses in Parasites (COSS)

When the MOSFET is turned off, the charge in the parasitic output capacitor (COSS) causes power to be dissipated.

Problems with the MOSFET's Body Diode's Reverse Recovery (Q_{rr} and V_{rr})

The return time (t_{rr}) of the body diode of the MOSFET is associated with these losses. By removing the extra charge (Q_{rr}) from the drift area prior to the diode junction becoming reverse-biased, the diode is able to switch off. The unwanted reverse recovery voltage (V_{rr}) is caused by this excess Q_{rr}.

The following formula encompasses the equation for switching losses in Three-Level Converters (TLC), Bidirectional Inverter Converters (BIC), and Conventional Buck/Boost Converters (CBC). It takes into account the cumulative influence of these distinct loss components. To characterize and reduce switching

losses in various converter designs, this comprehensive knowledge is crucial.

$$P_{sw} = f_s.N_{ps}.N_{pc}.\left(0.5.V_{DS}(t)I_D(t)\left(t_r + t_f\right) + 0.5.V_{DS}^2(t)C_{oss} + Q_tV_G\right) + V_{rr}(t)Q_{rr}) \quad (13)$$

The switching frequency, denoted as fs, is associated with the number of paralleled-switches (NPS) and parallel converter (Npc). For the CBC configuration, there are 6 paralleled-switches and 1 parallel converters. For the BIC configuration, there are 3 paralleled-switches and 2 paralleled converters. Lastly, for the TLC configuration, there are 2 paralleled-switches and 1 paralleled converter. Furthermore, the terms tr and tf represent the time it takes for MOSFETs to change from the low-to-high and high-to-low states, respectively, throughout switching intervals [24].

Dielectric Losses

Conduction loss, which is mostly caused by low switching frequencies, is measured by the MOSFET drain's RMS current (ISRMS) and on-state resistance (RDSon). The conduction loss for both CBC and BIC may be computed by the following formula.

$$P_{CDCBC-BIC} = N_{pc}.(R_{DS(on)}\frac{I_{SRMS}^2(t)}{N_{PS}} + N_{PS}V_FI_{Davg}(t)) \quad (14)$$

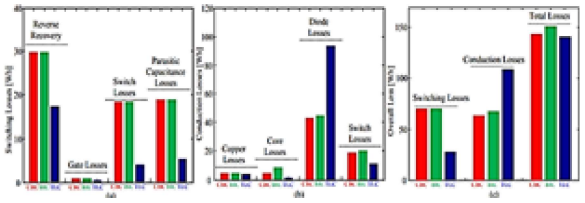

Fig. 9 Energy losses at a 20 kHz switching frequency a) Switching losses, b) core and conduction losses , c) and overall loss

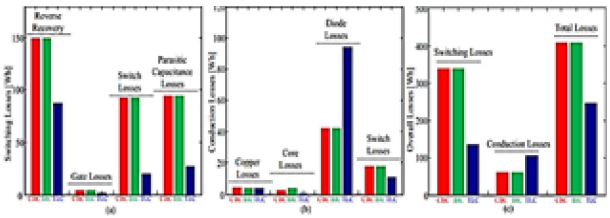

Fig. 10. Energy losses at 100 kHz switching frequency (a) Switching losses, (b) Conduction and core losses, (c) Overall loss

As indicated by Eq. (15), VF and IDavg are obtained by multiplying the core volume Ve and the core loss density Pe (Bac, fs), which are derived from the AC magnetic flux density Bac and the operating frequency fs.

$$P_{Cu} = V_eP_e(B_{ac}(t), f_s \quad (15)$$

The permeability indicated above (u_r = 60) was actually supplied by Magnetics Inc. for the calculation of Pe (Bac, f_s) using the Eq. (16) [25].

$$P_e(B_{ac}, f_s) = 193B_{ac}^{2.01}(t)\frac{f_s}{1000}^{1.29}{}_e \quad (16)$$

Efficiency Analysis

The converter losses are computed using Equations (14)–(16) taking into consideration the voltage profiles and dynamic power mentioned in the unit above. Fig. 9 displays the energy losses as a consequence for each of the three converters operating at a switching frequency of 20 kHz.

In a similar vein, parasitic capacitances MOSFETs have much reduced losses. For the specified switching frequency, gate losses are negligible. Fig. 9(b) shows the conduction losses, core losses, and copper losses shown. To begin with, TLC uses fewer switches than other converters, which means that its conduction losses are lower. On the other hand, when more diodes are used, the loss due to diode breakdown is greater. Fig. 9(c) displays the total losses of all converters. Despite having greater total conduction losses, TLC shows somewhat better efficiency than alternatives. In, you can see the outcomes at a switching frequency of 100 kHz [26].

The investigational waveforms for the TLC boost mode with a duty cycle (d) of 0.48 are shown in Fig. 10. There are three voltages involved in this system: 67V for the input, 130V for the output, and 500W for the output power. The waveforms show the following: a) the input voltage, output current, and voltages across switches S1 and S4; b) the voltages across switches S2 and S3; and c) the voltages across the inductor.

Fig.10. There is a clear indication that the efficiency gain is far larger here. This further demonstrates that greater switching frequencies make TLC more advantageous. It

is possible to calculate the converters' total efficiencies over the whole drive cycle by consulting therefore mentioned charts and doing the following:

$$\cap = \frac{P_o}{P_o + P_{SW} + P_{CD} + P_{CU} + P_C} \quad (17)$$

CBC has an efficiency of 98.7%, BIC of 98.5%, and TLC of 98.8%from Eq. (17). As the switching frequency increases to 100 kHz, the efficiencies decrease to 96.4%, 96.3%, and 98%, sequentially. The analysis revealed that, depending on the driving cycle conditions and the size of the magnetic components, TLC converters function more efficiently than CBC and BIC converters. A larger efficiency gap is produced by greater switching frequencies [27].

Control Complexity

Because it uses a single carrier signal to produce two PWM pulses, the control mechanism of a conventional buck/boost converter (CBC) is very simple because there are fewer switches. The Bidirectional Inverter Converter (BIC) and Three-Level Converter (TLC), on the other hand, need two carrier signals phase-shifted 180 degrees. Importantly, TLC and BIC are similar in that they both generate PWM. The existence of a floating ground makes TLC more complicated and expensive, as it requires independent gate drivers for three switches [28-29].

The neutral-point voltage balancing controller is the main source of complication in TLC control. Assuming perfect symmetry in the drive and main circuits, the DC link capacitor voltages should be half of the dc link voltage in an ideal world. However, DC bus capacitor Equivalent Series Resistance (ESR), drive circuit inhomogeneity, and switch asymmetry all contribute to the observed discrepancies. The result is that capacitor voltages are not uniform, this causes switches and dc-link capacitors to experience varying voltage strains. TLC thus needs a different voltage balancing control. Identifying the top or bottom capacitor voltage and adjusting S2 or S3's duty cycle in boost mode and S1 or S4's duty cycle in buck mode correspondingly is one effective technique. By using this compensating duty cycle, the switch's pulse width is changed in relation to its complimentary switch. This corrects voltage discrepancies in the dc link capacitors and guarantees that voltage stressors are distributed uniformly. When it comes to maximizing the TLC converter's performance and reliability in real-world operating situations, this complex control method is crucial [30-31].

RESULT AND DISCUSSION

A 1kW TLC proof-of-concept prototype has been painstakingly designed. The converter's 100 kHz switching frequency produces an effective ripple frequency of 200 kHz when it is in operation. In order to make this work, a 100µH inductor is chosen with great care. The IRFP350 switches used have a breakdown voltage of 400V and can handle a constant drain current of 16A. A low-priced dsPIC30f4011 microcontroller is employed for control functions. The current flowing via the inductor is tracked by an LEM CAS-25 sensor.

The outcomes in boost mode at three different operating points. Different voltages are applied to diodes and switches in each situation; significant voltage spikes are created by hard-switching and parasitic inductances on the PCB. As demonstrated by the findings for the switching frequency and the doubled inductor current frequency converter with the parameters indicated in Table 3, these contributions to oscillations become apparent at a system frequency of 200 kHz.

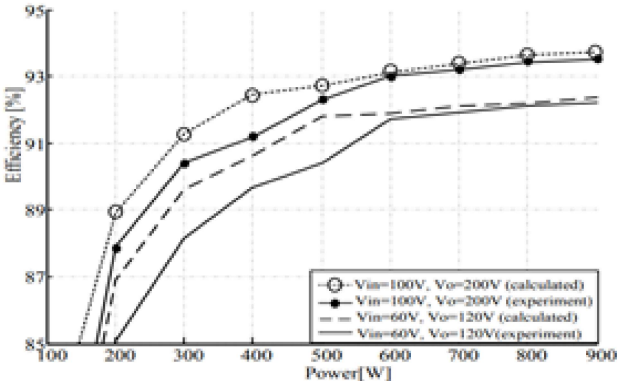

Fig. 11 Efficiency curve of the three-level converter

Fig. 11 shows the efficiency curves that were obtained from various voltage and power experiments. These curves were then compared with the calculated efficiencies that were also obtained under the same conditions. The accuracy of the created loss model is confirmed by this examination. At a switching frequency of 200 kHz and a power of 900W, the model's efficiency

curves remarkably match those seen experimentally, reaching a peak efficiency of 93.2%. This proves that the suggested loss model is accurate and dependable, and it shows that it can accurately forecast how the 1kW TLC converter would operate.

CONCLUSIONS

Because it significantly affects system size and efficiency in controlling battery power, the choice of bidirectional dc/dc converter architecture is crucial to the performance of battery/UC hybrid EV. The efficiency of the converter decreases with increasing switching losses, and this impact is more pronounced at higher switching frequencies. This study proposes a three-level non-isolated bidirectional dc/dc converter (TLC) as the power electronics interface between the battery and UC in place of the traditional two-quadrant buck/boost converter (CBC). This modification is anticipated to increase conversion efficiency and decrease the size of magnetic components.

The study focuses on the three-level converter in particular, comparing its magnetic component size and performance to that of CBC and interleaved bidirectional converters. UDDS drive cycles are used to test these parameters. The results show that the TLC converter has the smallest magnetic component size and is the most efficient while all of the driving cycle conditions are met, especially at high switching frequencies. Battery/UC hybrid EVs may benefit from the three-level, non-isolated bidirectional dc to dc converter architecture, as these features.

REFERENCE

1. M. Ortuzar, J. Moreno, and J. Dixon, "Ultracapacitor-Based Auxiliary Energy System for an Electric Vehicle: Implementation and Evaluation," IEEE Trans. on Ind. Electron., vol. 54, no. 4, pp. 2147-2156, Aug. 2007.
2. O. Laldin, M. Moshirvaziri, and O. Trescases, "Predictive Algorithm for Optimizing Power Flow in Hybrid Ultracapacitor/Battery Storage Systems for Light Electric Vehicles," IEEE Trans. on Power Electron., vol. 28, no. 12, pp. 3882-3895, Aug. 2013.
3. I. Aharon and A. Kuperman, "Topological Overview of Powertrains for Battery-Powered Vehicles With Range Extenders," IEEE Trans. on Power Electron., vol. 26, no. 3, pp. 868-876, Mar. 2011.
4. A. Khaligh and Z. Li, "Battery, Ultracapacitor, Fuel-cell, and Hybrid Energy Storage Systems for Electric, Hybrid Electric, Fuel Cell, and Plug-in Hybrid Electric Vehicles: State-of-Art," IEEE Trans. on Veh. Technol., vol. 59, no. 6, pp. 2806-2814, July 2010.
5. D. Rotenberg, A. Vahidi, and I. Kolmanovsky, "Ultracapacitor Assisted Powertrains: Modeling, Control, Sizing, and the Impact on Fuel Economy," IEEE Trans. on Control Systems Technol., vol. 19, no. 3, pp. 576-589, May. 2011.
6. W.-S. Liu, J.-F. Chen, T.-J. Liang, R.-L. Lin, and C.-H. Liu, "Analysis, Design, and Control of Bidirectional Cascoded Configuration for a Fuel Cell Hybrid Power System," IEEE Trans. on Power Electron., vol. 25, no. 6, pp. 1565-1575, Jun. 2010.
7. J. Jia, G. Wang, Y. T. Cham, Y. Wang, and M. Han "Electrical Characteristic Study of a Hybrid PEMFC and Ultracapacitor System," IEEE Trans. on Ind. Electron., vol. 57, no. 6, pp. 1945-1953, Jun. 2010.
8. M. H. Todorovic, L. Palma, and P. N. Enjeti, "Design of a Wide Input Range DC–DC Converter With a Robust Power Control Scheme Suitable for Fuel Cell Power Conversion," IEEE Trans. on Ind. Electron., vol. 55, no. 3, pp. 1247-1255, Mar. 2008.
9. Thakre, M. P., & Kumar, N. (2022). Design, Development, and Simulation Modeling of Hybrid Electric Vehicles Incorporating with BLDC Drive. In Planning of Hybrid Renewable Energy Systems, Electric Vehicles and Microgrid: Modeling, Control and Optimization (pp. 513-551). Singapore: Springer Nature Singapore.
10. A. Emadi, K. Rajashekara, S. S. Williamson, and S. M. Lukic, "Topological Overview of Hybrid Electric and Fuel Cell Vehicular Power System Architectures and Configurations," IEEE Trans. on Veh. Technol., vol. 54, no. 3, pp. 763–770, May 2005.
11. J. Bauman and M. Kazerani, "A Comparative Study of Fuel-cell-Battery Fuel-cell-Ultracapacitor and Fuel-cell-Battery-Ultracapacitor Vehicles," IEEE Trans. Veh. Technol, vol. 57, no. 2, pp. 760-769, Mar. 2008.
12. P. Thounthong, V. Chunkag, P. Sethakul, B. Davat, and M. Hinaje, "Comparative Study of Fuel-Cell Vehicle Hybridization with Battery or Supercapacitor Storage Device," IEEE Trans. Veh. Technol, vol. 58, no. 8, pp. 3892-3904, Oct. 2009.
13. U. R. Prasanna and A. K. Rathore, "Extended Range ZVS ActiveClamped Current-Fed Full-Bridge Isolated

DC/DC Converter for Fuel Cell Applications: Analysis, Design, and Experimental Results," IEEE Trans. on Ind. Electron., vol. 60, no. 7, pp. 2661–2672, Jul. 2013.

14. P. Xuewei and A. K. Rathore, "Novel Bidirectional Snubberless Naturally Commutated Soft-switching Current-fed Full-bridge Isolated DC/DC Converter for Fuel Cell Vehicles," IEEE Transactions on Ind. Electron., vol. 61, no. 5, pp. 2307-2315, 2014.
15. A. Khaligh and A. Emadi, "Mixed DCM/CCM pulse adjustment with constant power loads," IEEE Trans. on Aerospace and Electronic Systems, vol. 44, no. 2, pp. 766-782, Apr. 2008.
16. D. Yu, Z. Xiaohu, B. Sanzhong, S. Lukic, A. Huang, "Review of no isolated bi-directional DC-DC converters for plug-in hybrid electric vehicle charge station application at municipal parking decks," in Proc. IEEE Applied Power Electronics Conference and Exposition (APEC), pp. 1145-1151, 2010.
17. R. M. Schupbach and J. C. Balda, "Comparing DC-DC converters for power management in hybrid electric vehicles," in Proc. IEEE Electric Machines and Drives Conf. (IEMDC), pp. 1369-1374, 2003.
18. Shriwastava, R., Thakre, M. P., Choudhari, J., Kadlag, S. S., Mapari, R., Kadam, D. P., & Khule, S. (2023). Performance analysis of FOC space vector modulation DCMLI driven PMSM drive. Bulletin of Electrical Engineering and Informatics, 12(5), 2682-2692.
19. A. K. Rathore, "Interleaved soft-switched active-clamped L-L type current-fed half-bridge dc-dc converter," Int. Journal on Hydrogen Energy, vol. 34, no. 24, pp. 9802-9815, Dec 2009.
20. A. K. Rathore, and U. R. Prasanna, "Analysis, design, and experimental results of novel snubberless bi-directional naturally clamped ZCS/ZVS current-fed half-bridge dc/dc converter for fuel cell vehicles" IEEE Trans on Ind. Electron., vol. 60, no. 10, pp. 4482-4491, Oct. 2013.
21. P. J. Grbovic, P. Delarue, P. L. Moigne, and P. Bartholomeus, "A Bidirectional Three-Level DC-DC Converter for the Ultracapacitor Applications," IEEE Trans. on Ind. Electron., vol. 57, no. 10, pp. 3415–3430, Oct. 2010.
22. A. Shahin, M. Hinaje, J-P. Martin, S. Pierfederici, S. Rael, and B. Davat, "High Voltage Ratio DC-DC Converter for Fuel-Cell Applications," IEEE Trans. on Ind. Electron., vol. 57, no. 12, pp. 3944–3954, Dec. 2011.
23. L. Po-Wa, Y.-S. Lee, D. K. W. Cheng, and L. Xiu-Cheng, "Steady-state analysis of an interleaved boost converter with coupled inductors," IEEE Trans. on Ind. Electron., vol. 47 , no. 4, pp. 787 – 795, Aug. 2000.
24. H. Kosai, J. Scofield, S. McNeal, B. Jordan, and B. Ray," Design and Performance Evaluation of a 200 °C Interleaved Boost Converter," IEEE Trans. on Power Electron., vol. 28, no. 4, pp. 1691 – 1699, Apr. 2013.
25. S. Dusmez and A. Khaligh, "Wavelet-transform based energy and power decoupling strategy for a novel ultracapacitor-battery hybrid power split gear powertrain," in Proc. IEEE Transportation Electrification Conf. and Expo (ITEC), pp.1-7, 2013.
26. Gidd, A. R., Gore, A. D., Jondhale, S. B., Kadekar, O. V., & Thakre, M. P. (2019, April). Modelling, analysis and performance of a DSTATCOM for voltage sag mitigation in distribution network. In 2019 3rd International Conference on Trends in Electronics and Informatics (ICOEI) (pp. 366-371). IEEE.
27. B. Vural, S. Dusmez, M. Uzunoglu, E. Ugur, and B. Akin, "Fuel Consumption Comparison of Different Battery/Ultracapacitor Hybridization Topologies for Fuel-Cell Vehicles on a Test Bench," IEEE J. Emerg. and Sel. Topics in Power Electronics, Early Access, DOI: 10.1109/JESTPE.2013.2297702.
28. Thakre, M. P., Tapre, P. C., Kadlag, S. S., Kadam, D. P., Thorat, J. S., Nandeshwar, R. N., & Gaikwad, R. S. (2023). Implementation of a P&E management system for a dual-source EV powered by different batteries. Bulletin of Electrical Engineering and Informatics, 12(6), 3190-3201.
29. A. S. Samosir, and A. H. M. Yatim, "Implementation of Dynamic Evolution Control of Bidirectional DC–DC Converter for Interfacing Ultracapacitor Energy Storage to Fuel-Cell System," IEEE Trans. on Ind. Electron., vol. 57, no. 10, pp. 3468–3473, Oct. 2010.
30. S. Dusmez and A. Khaligh, "Generalized Technique of Compensating Low-Frequency Components of Load Current with Parallel Bidirectional DC/DC Converter," IEEE Trans. on Power Electronics, Early Access, DOI: 10.1109/TPEL.2014.2298432.
31. J. Dixon, I. Nakashima, E. F. Arcos, and M. Ortuzar, "Electric Vehicle Using a Combination of Ultracapacitors and ZEBRA Battery", IEEE Trans. Ind. Electron., vol. 57, no. 3, pp. 943-949, 2010.
32. A. Khaligh and S. Dusmez, "Comprehensive Topological Analysis of Conductive and Inductive

Charging Solutions for Plug-In Electric Vehicles," IEEE Trans. on Veh. Technol., vol. 61, no. 8, pp. 3475-3489, Oct. 2012.

33. J. Moreno, M. E. Ortuzar, J. W. Dixon, "Energy-management system for a hybrid electric vehicle, using ultracapacitors and neural networks," IEEE Trans. on Ind. Electron., vol. 53, no. 2, pp. 614-623, Apr. 2006.

34. A. A. Ferreira, J. A. Pomilio, G. Spiazzi, L. de Araujo Silva, "Energy Management Fuzzy Logic Supervisory for Electric Vehicle Power Supplies System," IEEE Trans. on Power Electron., vol. 23, no. 1, pp. 107-115, Jan. 2008.

35. S. Dusmez and A. Khaligh, "A Supervisory Power Splitting Approach for a New Ultracapacitor-Battery Vehicle Deploying Two Propulsion Machines," IEEE Trans. on Ind. Informatics, Early Access, DOI: 10.1109/TII.2014.2299237.

Using A Laser Security Application, An Automatic Gate System

Sagar Kawade
Department of Electrical Engineering
SVERI's College of Engineering
Pandharpur, Maharashtra
✉ sagarkawade844@gmail.com

Tejaswini Gaikwad
Assistant Professor
Department of Civil Engineering
SVERI's College of Engineering
Pandharpur, Maharashtra

Mohan Thakre
Associate Professor
Department of Electrical Engineering
SVERI's College of Engineering
Pandharpur, Maharashtra

Ranjana Khandebharad
Assistant Professor
Department of Electrical Engineering
SVERI's College of Engineering
Pandharpur, Maharashtra

ABSTRACT

This article uses an Arduino UNO, a buzzer, a laser light, and straightforward software for forming a security system. With this technology, we can set up a security alarm for unauthorized intruders anywhere. Safety is more and more important in all fields as technology develops and grows daily. Everyone wants their private area which only they can access. Therefore, we need to protect our room, office, locker, etc. The "Password-based gate lock system by using Arduino" has been created in the suggested work. This item is a password- or pin-protected computerized gate lock. Which requires the user to enter the proper password or PIN code to access the gate? In this paper, a basic IOT gateway implementation proposal for use in a home IOT environment is presented. It is based on the Arduino microcontroller. The author focused their study on the system's security and performance. The performance and capacity limits of the implemented gateway were examined through load experiments and denial-of-service attacks.

KEYWORDS *: Security system, Laser, Arduino, Face detention, IOT.*

INTRODUCTION

Considering the present scenario, security is a key consideration. Every day, new technology is developed worldwide. The criminal organization develops new technology to carry out its operations [1]. Therefore, security technology needs to be up-to-date and resilient to safeguard against crime. In this article, a vast area has been covered using laser light. We know laser light travels through long distances without scattering effects [2]. The conventional approach requires an excessive quantity of paperwork and is more prone to human error. By removing the drawbacks of conventional techniques and concentrating on enhancing their benefits, highlighting the most recent technical developments can help in the development of innovative systems. [3]. Here is a security device that makes use of a cheap laser torch that is typically included with a key chain. The benefit of this security lock is that any laser pointer or torch that is readily accessible in toy stores can be used [4].

Author J.A. Dharne's automatic gate management system utilizing number plate recognition and OCR: Every day, new technology is developed worldwide. The criminal gangs of today continue to advance their technology to run their business. Therefore, security technology must advance over time to keep the globe free from crime [5]. A microcontroller called Arduino Uno is employed in the suggested setup. In the suggested system, Arduino is primarily used to offer a platform for digital devices to connect with interactive items that can sense and control physical equipment. [6]. These two characteristics enable us to create a cutting-edge security system that we might refer to as the "Laser Security System. "Anytime a person or item passes in front of the laser light, the buzzer automatically sounds[7].Automatic railway gate management

by Chandan Ray using an Arduino [8]: Presently, transportation is a necessary mode of transportation that many people use regularly. The main focus of this post is the automatic railway gate control using Arduino UNO, buzzer, LED, IR sensor, etc.[9]. For additional safety purposes, a GSM module is used. Railways are one of those transportation mediums. Controlling automatic train gates with an Arduino Chandan Ray, the author in today's society, transportation has developed into an indispensable tool and is now a common part of many people's everyday lives. Railroads are one of those transportation modes, and this article primarily concentrates on railroad automation, specifica lly an Arduino UNO, a buzzer based automatic railway gate control [10]. You can more precisely control who has access to your property thanks to these tools. Automated gates increase protection and improve perimeter control. You can cut down on the likelihood of crimes like larceny and vandalism because you have control over who has access to your property [11].

Unauthorized access can be prevented by having a lock that holds the fingerprints of one or more users and opens the system when a match is found[12]. The skin on our hands and soles displays a flow-like pattern of ridges on each fingertip that is distinct and unchanging, making biometric authorization one of the greatest characteristics [13]. As a result, everyone may be identified by their fingerprints. Recent hand-held gadgets like mobile phones and computers feature fingerprint scanners, which makes it simple to infer their popularity and dependability [14]. With biometrics, a special pattern will be utilized as the key. We will utilize a fingerprint as the key in this case to implement the article. The security lock will be implemented using a variety of gadgets, each with a unique function to raise the level of security, in this Arduino article [15].

Simply put, we might say that we are using Arduino to create a door access system that analyzes fingerprints to decide who we should let inside and who we shouldn't. To keep the device's price as low as possible, we are attempting to create it using a typical, basic door lock that is installed in every home [16]. One kind of security system that uses lasers to find intruders is a laser security system. The device operates by directing a laser beam through a room or other area and then detecting any disturbances in the beam caused by an intruder [17]. If the beam is disturbed, an alarm is triggered, alerting the owner of the system to the presence of an intruder. Laser security systems are often used in high-security environments, such as banks, museums, and government buildings. For deployment, experimental results and Simulation can be used, and the modeling results indicate the improved proposed controller performance[18]. This paper describes in the following sections, the methodology that is adopted, some of the reviews based on observation, and the overall conclusion which has the base of previous sections.

METHODOLOGY

This section goes into great depth about the processes and methods used in the conception, creation, and use of an automatic gate. The automated gate was constructed using both mechanical and electronic components. The single-phase electric motor, the Arduino Uno IR sensor buzzer, and the relay circuit are the electrical parts used to build the control circuit for the automatic gate Magnetic connections; and control keys for both heat overload valves and circuit breakers. Cables, breakers, an alert circuit, and signal lights [19] [20].

Creating a fingerprint-based security system using an Arduino board and a fingerprint sensor is important because thefts are getting worse daily, and security has become a key issue. Therefore, securing our home or locker is made simple by a digital fingerprint lock [21] You'll be able to follow the proper fingerprint entry. A fingerprint-based door lock system allows only authorized people access to the restricted ones. The entire article is controlled by the Arduino [22].

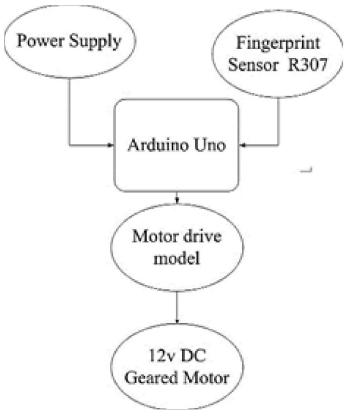

Fig. 1 Laser Security & Automatic Gate Way System

Arduino UNO

The Arduino UNO is the best board for learning to code and solder circuits. If this is your first experience experimenting with the platform, the UNO is the most robust board you could start with. The most well-known and thoroughly documented device in the Arduino family is the UNO board. [23]. This is made with the open-source Arduino platform. With Arduino, you can use a piece of software called the IDE (Integrated Development Environment) that runs on your computer to create and upload computer code to a physical programmable circuit board, also known as a microcontroller [24].

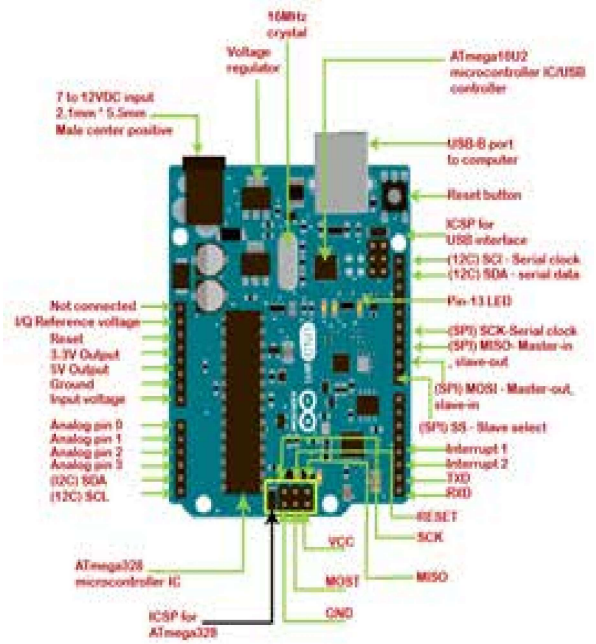

Fig. 2 Arduino UNO

The Arduino may be programmed and started from a different location via these pins. These pins facilitate communication between multiple Arduino boards and enable firmware uploading. When programming or starting the Arduino, the ICSP pins function like an AVR programmer [25]. The Arduino board itself has a push button on top that is designated as the RESET key. It may be blue or white. Pressing it has the same effect as turning the power source on and off again [26]. The board will not begin executing any of the instructions in the sketch until after a new design has been uploaded.

A TTL-USB converter is needed for direct module connection to the PC without an intermediary microcontroller or comparable platform. The LM358 may be used as a DC gain block and transducer amplifier. A voltage regulator is a part that delivers a constant output voltage regardless of variations in the input voltage. A three or more-pin integrated circuit (IC) is what it is. The Arduino's digital inputs (also known as digital I/O) are what enable you to connect other integrated circuits (ICs), actuators, and sensors to the board. When a barrel plug is put into the jack, the jack's spring pulls against the plug's outer sleeve, forcing the jack's central pin to make contact with the plug's inner sleeve.

With its on-chip trimming, this fixed regulator can achieve its voltage output tolerance of 1% while offering much protection and stability for your article. These voltage regulators each have a maximum output current of 800 mA.This fixed regulator offers excellent stability and safety for your article, and because of its on-chip trimming, it can achieve an output voltage accuracy of less than 1%. Each of these regulators for voltage has a maximum output current capacity of 800 mA [27].

The Multi-Flex's Tx and Rx LEDs show whether it is transmitting or receiving messages over the RS485 network. Each time the multi-flex responds to the E2 by sending a signal, the Tx LED blinks once. When a message is received by the Multi-Flex, the Rx LED blinks once.

Resonators perform similarly to crystals but are less expensive and do not need additional caps. The temperature range for these resonators is +/-0.5% or better. There is no need for external caps because these resonators contain built-in load capacitors [28].

ICSP for ATMege328p

ICSP programming is a method of programming microcontrollers while they are still connected to a circuit. This allows for the programming of the microcontroller without having to remove it from the circuit. The Atmega328p microcontroller, which is commonly used in Arduino boards, can be programmed using the ICSP method. The programming is done through six pins on the microcontroller that are used to transfer data and commands [29].

ATmega328p Microcontroller

The ATmega328P is a microcontroller that is commonly used in Arduino boards. This 8-bit, low-power CMOS microcontroller has AVR upgrades and is based on the RISC architecture [30]. It features 32KB of flash memory, 2KB of SRAM, and 1KB of EEPROM for non-volatile data storage, together with 32KB of flash memory for storing code. It contains 6 analog inputs, 23 general-purpose I/O pins, 6 PWM output pins, and 6 general-purpose I/O pins. It also has a variety of communication interfaces, including SPI, 12C, and USART. The ATmega328P is a versatile microcontroller that is used in a wide range of applications, from robotics to home [31].

Analogue inputs

The Arduino can input and output analog signals in addition to digital signals. An analog signal can have any number of values, in contrast to a digital signal, which only has two values: HIGH and LOW.

Motor drive model

CPU: ESP8266(LX106) Community Developer: ESP8266 Opensource Introductory Power:

The L293 is a popular motor driver IC that can control two DC motors or one stepper motor. It is an H-bridge driver, which means that it can control the direction of the motor by reversing the polarity of the voltage applied to it. The L293 can handle a maximum current of 600mA per channel and can operate on a wide range of voltages, from 4.5V to 36V. It also has built-in protection diodes that prevent damage to the IC from the back EMF generated by the motor. The L293 is commonly used in robotics, automation, and other applications that require motor control [32]. There are more nonlinear loads in the system, which introduce harmonics and cause a variety of power quality issues [33].

Fig. 3 Motor drive model

Finger-prints sensor R307

The fingerprint sensor module shown in the accompanying image made it easier and more economical to include fingerprint identification in this article [34]. This suggests that collecting, registering, comparing, and searching for fingerprints is fairly straightforward. These modules can store fingerprints in FLASH memory and may be used with any microcontroller or TTL serial system [35]. These elements can be included in security systems. the door locks, the clocks.

Fig. 4 Finger-prints sensor R307

12 V DC geared motor

A DC motor is any spinning electric motor that generates mechanical energy using direct current (DC) power. The most common types rely on the forces produced by the generated magnetic fields that the coil's current induces. To keep the intended DC working voltage, a finite energy storage capacitor terminates the voltage-sourced converter on the DC side. Therefore, the converter's functioning switch array serves as the conduit via which the DC capacitor communicates with the AC system.By injecting both current and voltage into the line at a subsynchronous frequency component, network damping may be increased. to occasionally change the current's direction in a particular section of the motor [36], Nearly every kind of DC motor has an internal mechanism. This system might be electrical or electromechanical. The functioning of a brushed electric motor including a two-pole rotor (armature) and a permanent magnet stator. On the magnets' inside axis faces, polarities are indicated by the letters "N" and "S"; the opposing polarities are shown on the outer faces.

Fig. 5 12 V DC geared motor

LDR Sensor

LDR Sensor Light Resistance: 50-100 Ohms LDR Rated Power: 200 W, Diameter: 3-20 mm, Application: Phot- resistor.

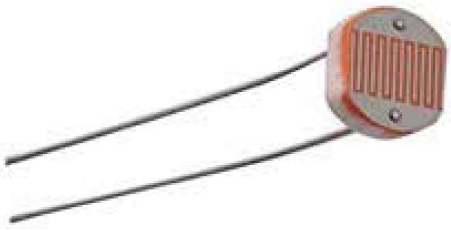

Fig. 6 LDR Sensor

Laser

A laser is a technology that causes light to be emitted at specific wavelengths and then amplifies that light, creating a highly narrow beam of radiation. Visible, infrared, or ultraviolet wavelengths are often only briefly covered by the emission. The features of the many distinct types of lasers that have been produced are quite diverse. The word "laser" is an abbreviation for "light amplification by the stimulated emission of radiation [37].

Fig. 7 Laser

Fingerprint Sensor Interface

Over half of all biometric safety devices use fingerprint scanning, the most used biometric technology, and it is easy to see why. We save an ever-increasing amount of data on the devices we use and distribute it in ever-more-dangerous ways online. Most of the time, simply a few hurriedly selected digits are used in our passwords to safeguard our financial and personal data.

The fingerprint sensor works on the principle of processing which includes two elements enrolment & matching. In enrolment, each individual has to put the finger on the sensor device, so that the device checks the fingerprints to process & generate the finger pattern & it will be stored [42]. In matching, once an individual places the finger then the system will generate a pattern of the finger &compare it with the stored data. So a fingerprint sensor is used to authenticate and recognize the fingerprints of a person. These sensors are very reliable and secure devices used for any security authentication [43].

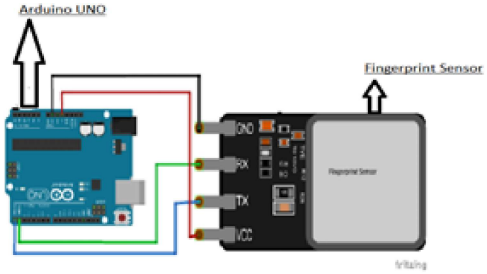

Fig. 8 Fingerprint sensor

Laser Security

A laser-based security system is one kind of security system that uses lasers to detect intruders. The system which works by emitting a laser beam across a room or other area and then detecting any disturbances in the beam caused by an intruder [44].

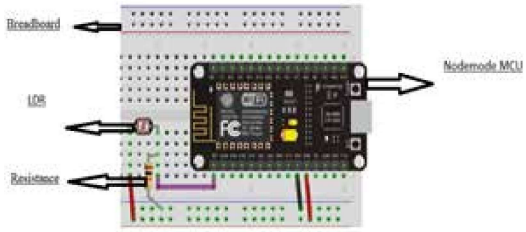

Fig. 9 Fingerprint sensor

If the beam is disturbed, an alarm is triggered, alerting the owner of the system to the presence of an intruder. Laser security systems are often used in high-security environments, such as banks, museums, and government buildings [45]

RESULT AND ANALYSIS

This section goes into great length regarding the steps involved in designing, building, and utilizing an automatic gate [38]. The control circuit for the automated gate was created using electric motors, Arduino Uno IR sensors, buzzers, and relay circuits. Control switches and a contractor. Circuit breaker and thermal overflow relay. Circuit breakers, signal lights, cables, and an alert system [39]. The metal framing, the metal gear in the gate rack, the rollers, the cantilever rollers, the counterbalance post, the last post, and the counterbalance are a few of the mechanical components used in the design and construction of an automated gate.

Fig 10 Laser Security Result

We are demonstrating the parts for the Arduino-based fingerprint gate lock and connecting them to the power source [40]. This approach is based on enhancing security and registers the owner's fingerprint into the Arduino using a fingerprint sensor. The cable used for uploading code has also been utilized to supply the Arduino with 5 volts of electricity. After signing in, placing your thumb on the fingerprint sensor will release the solenoid lock. This will cause the solenoid lock to lock if you repeat it. Since locking and unlocking the solenoid lock takes less than one second, it is used in this article [41].

OBSERVATIONAL CASES

Case 1: The lock will open

Fig 11 Automatic Gate lock will be open condition

In this system, the gate latch is connected to the fingerprint scanner, which the user will input their fingerprints into. The machine scans the print, and then searches its database for a match. If a match is discovered, the latch releases, unlocking the gate [46]. The user has the same issue while trying to lock the door. If the fingerprint is accurate, the latch will close and the gate will lock behind the person.

Case 2: The lock will not open

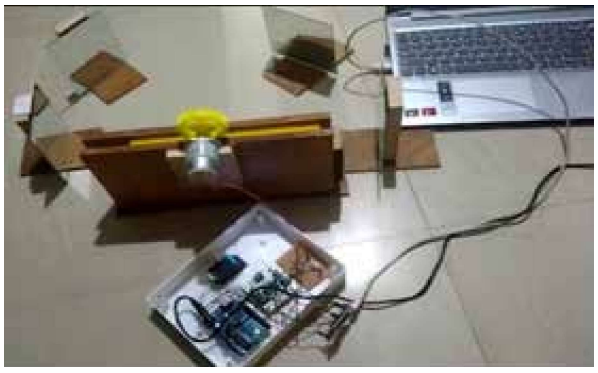

Fig 12: Automatic Gate lock will be not an open condition

The door will remain locked if the fingerprint is entered incorrectly, forcing the user to retry until the door is opened. If the wrong fingerprint is scanned, the user will be informed to restart immediately [47].

CONCLUSION

The methods used in the design, construction, and use of an automatic gate are covered in great depth in this section. The control circuit for the automated gate was created using electric motors, Arduino UNO, IR sensors,

buzzers, and relay circuits. Control switches and a magnetic contactor. Relay for thermal overload and circuit breaker. cables, alarm systems, circuit breakers, and signal lights. Some of the mechanical elements used in the design and building of an automatic gate include the metal framing, the gate rack metal gear, the rollers, the cantilever rollers, and the counterbalance.

Since each fingerprint is distinct, the sensor can recognize every print during testing. It gives access to sites that are prohibited more control. This system has various downsides, including the fact that it is a closed system and is challenging to modify in terms of hardware. Additionally, it requires a lot of electricity to run, making it occasionally difficult to supply constant power using batteries. It won't operate if there's a power outage. In such a scenario, we may either connect the system to an IPS or upgrade the system with rechargeable batteries.

REFERENCE

1. Andress, J., & Winterfeld, S. (2013). Cyber warfare: techniques, tactics and tools for security practitioners. Elsevier.
2. Iakovou, E., Vlachos, D., & Xanthopoulos, A. (2009). Risk and security management for logistics service providers: Trends, challenges and opportunities. Managing risk and security: The safeguard of long-term success for logistics service providers, 59-81.
3. Wakchoure, S. S., Shewale, P. S., Rajput, J. G., Gaupal, S. A., Thakre, M. P., & Rade, M. R. (2022). Multiple approaches of RFID-based attendance system using IoT. In Soft Computing for Security Applications: Proceedings of ICSCS 2021 (pp. 487-499). Springer Singapore.
4. Vrablic, M. E. (2020). TactionTablet: affordable tactile graphics display (Doctoral dissertation, Massachusetts Institute of Technology).
5. Clinton, B. (1998). A national security strategy for a new century. White House.
6. Thakre, M. P., Borse, P. S., Matale, N. P., & Sharma, P. (2021, January). IOT-based smart vehicle parking system using RFID. In 2021 International Conference on Computer Communication and Informatics (ICCCI) (pp. 1-5). IEEE.
7. d'Hont, S. (2004). The cutting-edge of RFID technology and applications for manufacturing and distribution. Texas Instrument TIRIS, 16.
8. Sharma, N., Pandey, P., Sarkar, U., & Jaiswal, N. (2019). An Approach For Cost Effective Security System Using Wireless Sensor Network. Think India Journal, 22(3), 7834-7848.
9. Iftekharuzzaman, I., Ghosh, S., Basher, M. K., Islam, M. A., Das, N., Nur-E-Alam, M., & Wang, D. (2023). Design and Concept of Renewable Energy Driven Auto-Detectable Railway Level Crossing Systems in Bangladesh..
10. João Karthick, N., Nagarajan, R., Suresh, S., & Prabhu, R. (2017). Implementation of railway track crack detection and protection. International Journal Of Engineering And Computer Science (IJECS), 6(5), 21476-21481.
11. Manzi, T., & Smith-Bowers, B. (2005). Gated communities as club goods: segregation or social cohesion?. Housing Studies, 20(2), 345-359.
12. Sarma, M., Gogoi, A., Saikia, R., & Bora, D. J. (2020). Fingerprint-based door access system using Arduino. Int. J. Sci. Res. Eng. Manage.(IJSREM), 4(8), 1-5.
13. Paul, P., Al Achib, M. A., Hossain, H. S., & Hossain, M. K. (2019). Smart Door Lock Using Fingerprint Sensor. BRAC University, 1-13.
14. Laoudias, C., Moreira, A., Kim, S., Lee, S., Wirola, L., & Fischione, C. (2018). A survey of enabling technologies for network localization, tracking, and navigation. IEEE Communications Surveys & Tutorials, 20(4), 3607-3644.
15. Rajee, T. C. A. FINGERPRINT DOOR LOCK USING ARDUINO.
16. Islam, M. W., Roy, B., Preety, N. H., & Mahtab, F. B. (2017). Design of Arduino based home automation systems incorporating identity detection (Doctoral dissertation, BARC University).
17. Schmid, D., & Stanton, N. A. (2018). How are laser attacks encountered in commercial aviation? A hazard analysis based on systems theory. Safety science, 110, 178-191.
18. Saravanan, S., Usha Rani, P., & Thakre, M. P. (2022). Evaluation and improvement of a transformerless high-efficiency DC–DC converter for renewable energy applications employing a fuzzy logic controller. MAPAN, 37(2), 291-310.

19. Ikpeze, O. F., Uwaezuoke, E. C., Samiat, B., & Kareem, K. M. (2019). Design and construction of an automatic gate. ABUAD J. Eng. Res. Dev, 2(2), 123-131.

20. GARG, A. K. (2017). Wireless Sensor Network Based Controlling And Monitoring Of Home Appliances Using Zigbee (Doctoral Dissertation).

21. Hayward, S. J., van Lopik, K., Hinde, C., & West, A. A. (2022). A survey of indoor location technologies, techniques and applications in industry. Internet of Things, 100608.

22. Tippannavar, S. S., Yashwanth, S. D., & Madappa, E. A. Two Factor Authentication using RFID and Biometric Sensor–A Progressive Review.

23. Pena, J. (2020). Promoting Computational Grounding Through Informal Coding Workshops for Non-programmers.

24. Fezari, M., & Al Dahoud, A. (2018). Integrated development environment "IDE" for Arduino. WSN applications, 1-12.

25. Okafor, K. C., Ononiwu, G. C., Precious, U., & Godis, A. C. (2017). Development of Arduino-based IoT metering system for on-demand energy monitoring. International Journal of Mechatronics, Electrical and Computer Technology, 7(23), 3208-3224.

26. Schubert, T. W., D'Ausilio, A., & Canto, R. (2013). Using Arduino microcontroller boards to measure response latencies. Behavior research methods, 45, 1332-1346.

27. Lefurgy, C. R., Drake, A. J., Floyd, M. S., Allen-Ware, M. S., Brock, B., Tierno, J. A., & Carter, J. B. (2011, December). Active management of timing guardband to save energy in POWER7. In Proceedings of the 44th Annual IEEE/ACM International Symposium on Microarchitecture (pp. 1-11).

28. Kojima, Y., Fujiwara, Y., Yamada, S., & Wakatsuki, N. 38th Annual Frequency Control Symposium. 1984. In OF THE 38th ANNUAL FREQUENCY CONTROL SYMPOSIUM (p. 114).

29. Blum, J. (2019). Exploring Arduino: tools and techniques for engineering wizardry. John Wiley & Sons.

30. Ali, A. S., Zanzinger, Z., Debose, D., & Stephens, B. (2016). Open Source Building Science Sensors (OSBSS): A low-cost Arduino-based platform for long-term indoor environmental data collection. Building and Environment, 100, 114-126.

31. Roslin, S. E., Soundar, P., Surendar, R., & Kannan, C. (2023). Design And Development Of Surveillance Rover For Border Security. EPRA International Journal of Research and Development (IJRD), 8(3), 191-196.

32. Roy, T. S., Kabir, H., & Chowdhury, M. A. M. (2014). Simple Discussion on Stepper Motors for the Development of Electronic Device. International Journal of Scientific & Engineering Research, 5(1), 1089-1096.

33. Gidd, A. R., Gore, A. D., Jondhale, S. B., Kadekar, O. V., & Thakre, M. P. (2019, April). Modelling, analysis and performance of a DSTATCOM for voltage sag mitigation in distribution network. In 2019 3rd International Conference on Trends in Electronics and Informatics (ICOEI) (pp. 366-371). IEEE.

34. Baidya, J., Saha, T., Moyashir, R., & Palit, R. (2017, January). Design and implementation of a fingerprint based lock system for shared access. In 2017 IEEE 7th Annual Computing and Communication Workshop and Conference (CCWC) (pp. 1-6). IEEE.

35. Win, Y. M., Nyein, S. A., & Aung, S. (2019). Wireless student attendance system using fingerprint sensor. Int. J. Trend Sci. Res. Develop.(IJTSRD).

36. Koteswara Raju, D., Umre, B. S., Junghare, A. S., Thakre, M. P., Motamarri, R., & Somu, C. (2016). Fractional-order PI based STATCOM and UPFC controller to diminish subsynchronous resonance. SpringerPlus, 5, 1-20.

37. Kim, M. M., & Darafsheh, A. (2020). Light sources and dosimetry techniques for photodynamic therapy. Photochemistry and photobiology, 96(2), 280-294.

38. Eastman, C. M. (2011). BIM handbook: A guide to building information modeling for owners, managers, designers, engineers and contractors. John Wiley & Sons.

39. Ali, Z., Sheikh, M. F., Al Rashid, A., Arif, Z. U., Khalid, M. Y., Umer, R., & Koç, M. (2023). Design and development of a low-cost 5-DOF robotic arm for lightweight material handling and sorting applications: A case study for small manufacturing industries in Pakistan. Results in Engineering, 101315.

40. Ikpeze, O. F., Uwaezuoke, E. C., Samiat, B., & Kareem, K. M. (2019). Design and construction of an automatic gate. ABUAD J. Eng. Res. Dev, 2(2), 123-131.

41. Peng, C., Chen, M., & Jiang, X. (2021). Under-display ultrasonic fingerprint recognition with finger vessel imaging. IEEE Sensors Journal, 21(6), 7412-7419.

42. Shoewu, O., & Idowu, O. A. (2012). Development of attendance management system using biometrics. The Pacific Journal of Science and Technology, 13(1), 300-307.

43. Bhattacharyya, D., Ranjan, R., Alisherov, F., & Choi, M. (2009). Biometric authentication: A review. International Journal of u-and e-Service, Science and Technology, 2(3), 13-28.

44. Schmid, D., & Stanton, N. A. (2018). How are laser attacks encountered in commercial aviation? A hazard analysis based on systems theory. Safety science, 110, 178-191.

45. Ball, S., Andrew, P., & Winsor, P. (2009). Larger & working objects: a guide to standards in their preservation and care. Collection Trust.

46. Blitz, M. J. (2003). Video surveillance and the constitution of public space: Fitting the fourth amendment to a world that tracks image and identity. Tex. L. Rev., 82, 1349.

47. Shim, J., Qureshi, A. A., & Siegel, J. G. (2013). The international handbook of computer security. Routledge.